NASA/TM—2003–212343

Hybrid Residual Flexibility/Mass-Additive Method for Structural Dynamic Testing

M.L. Tinker
Marshall Space Flight Center, Marshall Space Flight Center, Alabama

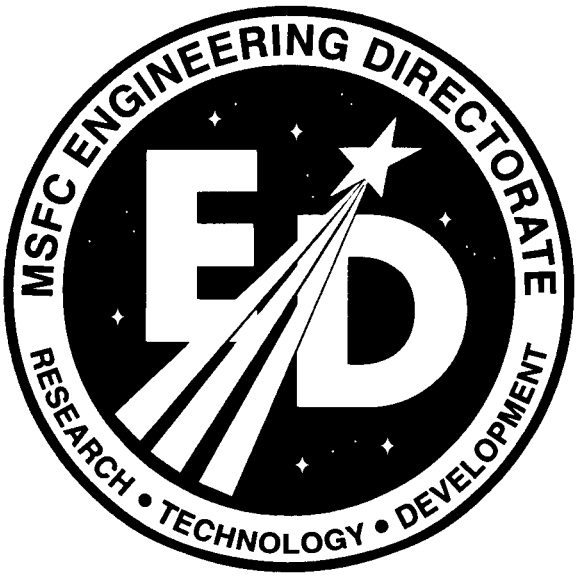

March 2003

The NASA STI Program Office...in Profile

Since its founding, NASA has been dedicated to the advancement of aeronautics and space science. The NASA Scientific and Technical Information (STI) Program Office plays a key part in helping NASA maintain this important role.

The NASA STI Program Office is operated by Langley Research Center, the lead center for NASA's scientific and technical information. The NASA STI Program Office provides access to the NASA STI Database, the largest collection of aeronautical and space science STI in the world. The Program Office is also NASA's institutional mechanism for disseminating the results of its research and development activities. These results are published by NASA in the NASA STI Report Series, which includes the following report types:

- TECHNICAL PUBLICATION. Reports of completed research or a major significant phase of research that present the results of NASA programs and include extensive data or theoretical analysis. Includes compilations of significant scientific and technical data and information deemed to be of continuing reference value. NASA's counterpart of peer-reviewed formal professional papers but has less stringent limitations on manuscript length and extent of graphic presentations.

- TECHNICAL MEMORANDUM. Scientific and technical findings that are preliminary or of specialized interest, e.g., quick release reports, working papers, and bibliographies that contain minimal annotation. Does not contain extensive analysis.

- CONTRACTOR REPORT. Scientific and technical findings by NASA-sponsored contractors and grantees.

- CONFERENCE PUBLICATION. Collected papers from scientific and technical conferences, symposia, seminars, or other meetings sponsored or cosponsored by NASA.

- SPECIAL PUBLICATION. Scientific, technical, or historical information from NASA programs, projects, and mission, often concerned with subjects having substantial public interest.

- TECHNICAL TRANSLATION. English-language translations of foreign scientific and technical material pertinent to NASA's mission.

Specialized services that complement the STI Program Office's diverse offerings include creating custom thesauri, building customized databases, organizing and publishing research results...even providing videos.

For more information about the NASA STI Program Office, see the following:

- Access the NASA STI Program Home Page at ***http://www.sti.nasa.gov***

- E-mail your question via the Internet to help@sti.nasa.gov

- Fax your question to the NASA Access Help Desk at (301) 621–0134

- Telephone the NASA Access Help Desk at (301) 621–0390

- Write to:
  NASA Access Help Desk
  NASA Center for AeroSpace Information
  800 Elkridge Landing Road
  Linthicum Heights, MD 21090–2934

NASA/TM—2003–212343

Hybrid Residual Flexibility/Mass-Additive Method for Structural Dynamic Testing

M.L. Tinker
Marshall Space Flight Center, Marshall Space Flight Center, Alabama

National Aeronautics and
Space Administration

Marshall Space Flight Center • MSFC, Alabama 35812

March 2003

Acknowledgments

Kathy Kappus, Tim Driskill, and Blane Anderson, of the Structural and Dynamics Testing Group at Marshall Space Flight Center, are acknowledged for their support of this project. They have participated extensively in studies of the residual flexibility, mass additive, and hybrid test techniques by providing modal and frequency response data for the payload simulator structure described in this Technical Memorandum (TM), as well as other structures. Kathy Kappus arranged for fabrication of the rectangular boundary mass discussed in this TM and provided the experimental frequency response functions used in section 4.

Eric Blades, formally of Structural Dynamics Research Corporation (SDRC) in San Diego, California, and currently at Mississippi State University, developed the FORTRAN computer code implementation of the hybrid equations developed in this TM. He also performed the initial computer simulations upon which many of the results in section 3 are based.

Available from:

NASA Center for AeroSpace Information
7121 Standard Drive
Hanover, MD 21076–1320
(301) 621–0390

National Technical Information Service
5285 Port Royal Road
Springfield, VA 22161
(703) 487–4650

TABLE OF CONTENTS

LIST OF FIGURES

LIST OF FIGURES (Continued)

LIST OF TABLES

LIST OF TABLES (Continued)

TECHNICAL MEMORANDUM

HYBRID RESIDUAL FLEXIBILITY/MASS-ADDITIVE METHOD FOR STRUCTURAL DYNAMIC TESTING

1. INTRODUCTION AND BACKGROUND

A large fixture was designed and constructed for modal vibration testing of *International Space Station* elements. This fixed-base test fixture, which weighs thousands of pounds and is anchored to a massive concrete floor, initially utilized spherical bearings and pendulum mechanisms to simulate Shuttle orbiter boundary constraints for launch of the hardware.[1] Many difficulties were encountered during a checkout test of the common module prototype structure, mainly due to undesirable friction and excessive clearances in the test-article-to-fixture interface bearings. Measured mode shapes and frequencies were not representative of orbiter-constrained modes due to the friction and clearance effects in the bearings. As a result, a major redesign effort for the interface mechanisms was undertaken. The total cost of the fixture design, construction and checkout, and redesign was over $2 million.

Because of the problems experienced with fixed-base testing, alternative free-suspension methods were studied, including the residual flexibility and mass-additive approaches. Free-suspension structural dynamics test methods utilize soft elastic "bungee" cords and overhead frame suspension systems that are less complex and much less expensive than fixed-base systems. The cost of free-suspension fixturing is on the order of tens of thousands of dollars, as opposed to millions, for large fixed-base fixturing. In addition, free-suspension test configurations are portable, allowing modal tests to be done at sites without modal test facilities. For example, a mass-additive modal test of the ASTRO–1 Shuttle payload was done at the Kennedy Space Center launch site.[2] In the following sections, the mass-additive and residual flexibility test methods are described in detail. A discussion of a hybrid approach that combines the best characteristics of each method follows and is the focus of study described in this Technical Memorandum (TM).

1.1 Mass-Additive Modal Test Method

It is well known that, for coupled substructures, the interfaces must be adequately characterized to allow accurate transient response and operational loads analyses. This is especially true for Shuttle payloads that are constrained at a number of discrete points (fig. 1). The dynamic response of the payload is largely controlled by the stiffness of the interfaces (trunnions and keel). For this reason, one of the primary objectives of modal testing of Shuttle payloads is to measure interface characteristics so that the mathematical model can be refined at the interfaces.

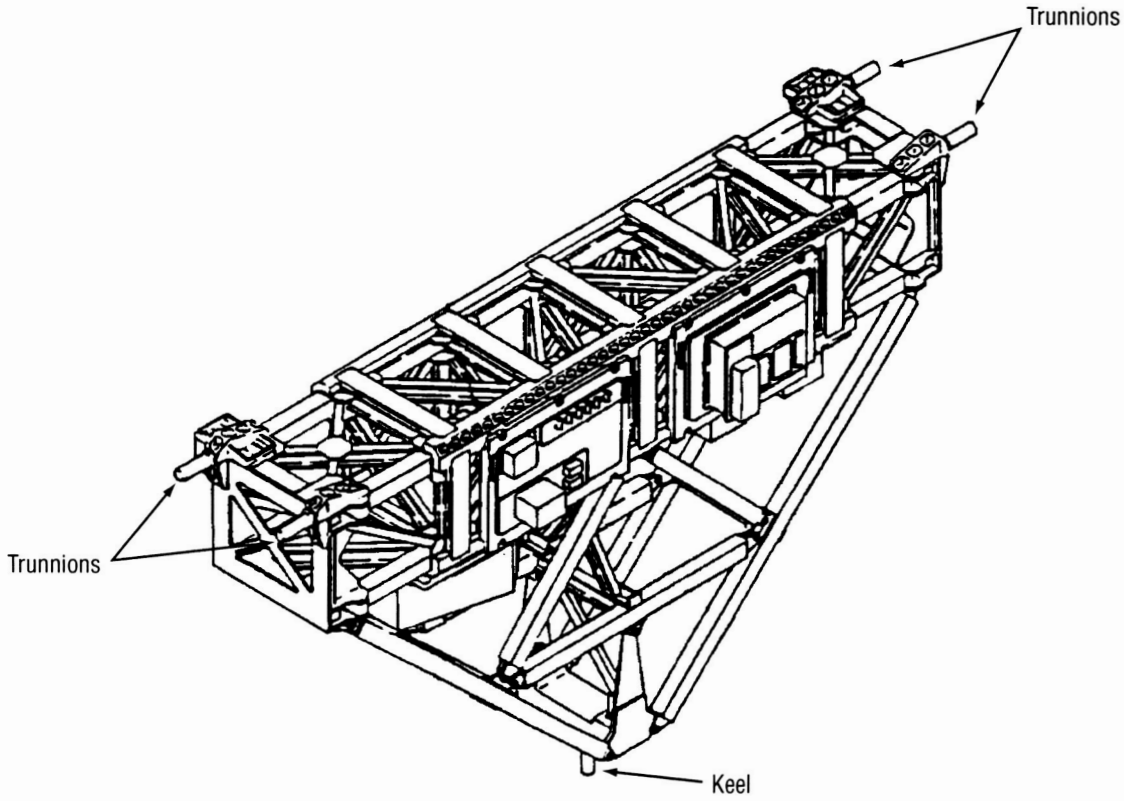

Figure 1. Shuttle payload carrier with orbiter connections.

Obviously, a constrained-boundary test allows direct measurement of the modes that are controlled by the interfaces. However, in a free-boundary support configuration, the interface modes occur at higher frequency than the structure global modes. Due to the large frequency bandwidth involved, this increases the time required to measure both the local interface modes and the global modes in one test. Further, it is difficult to develop a mathematical model with fidelity over a large frequency range.

In the mass-additive technique,[2–8] the structure boundaries are mass loaded to lower the frequencies of the interface modes and bring the modes into the frequency bandwidth of the global modes. This allows global free-free modes and the local interface modes to be easily measured in a single test. The idea of attaching masses to structure boundary degrees of freedom (DOFs) in modal testing is similar to the concept presented by Benfield and Hruda[9] for modal synthesis. A Shuttle payload with mass-loaded boundaries is shown in figure 2. In addition to narrowing the frequency bandwidth, the added masses allow the interfaces to be exercised to a greater degree than is possible in a usual free-boundary configuration. Interface modes are obtained due to extensive excitation of the structure in the interface regions.

From a modeling standpoint, the added masses are easily included as rigid bodies having known mass and inertia attached to the boundary DOFs. Constrained-boundary modes and frequencies can be obtained from a finite element model that has been updated to agree with measured free-free mass-additive modal data. First the masses are analytically removed from the updated model, then the boundary DOFs are constrained. Alternatively, the test-verified model with boundary masses removed can be coupled to a model of the launch vehicle and used for liftoff and/or landing loads analysis.

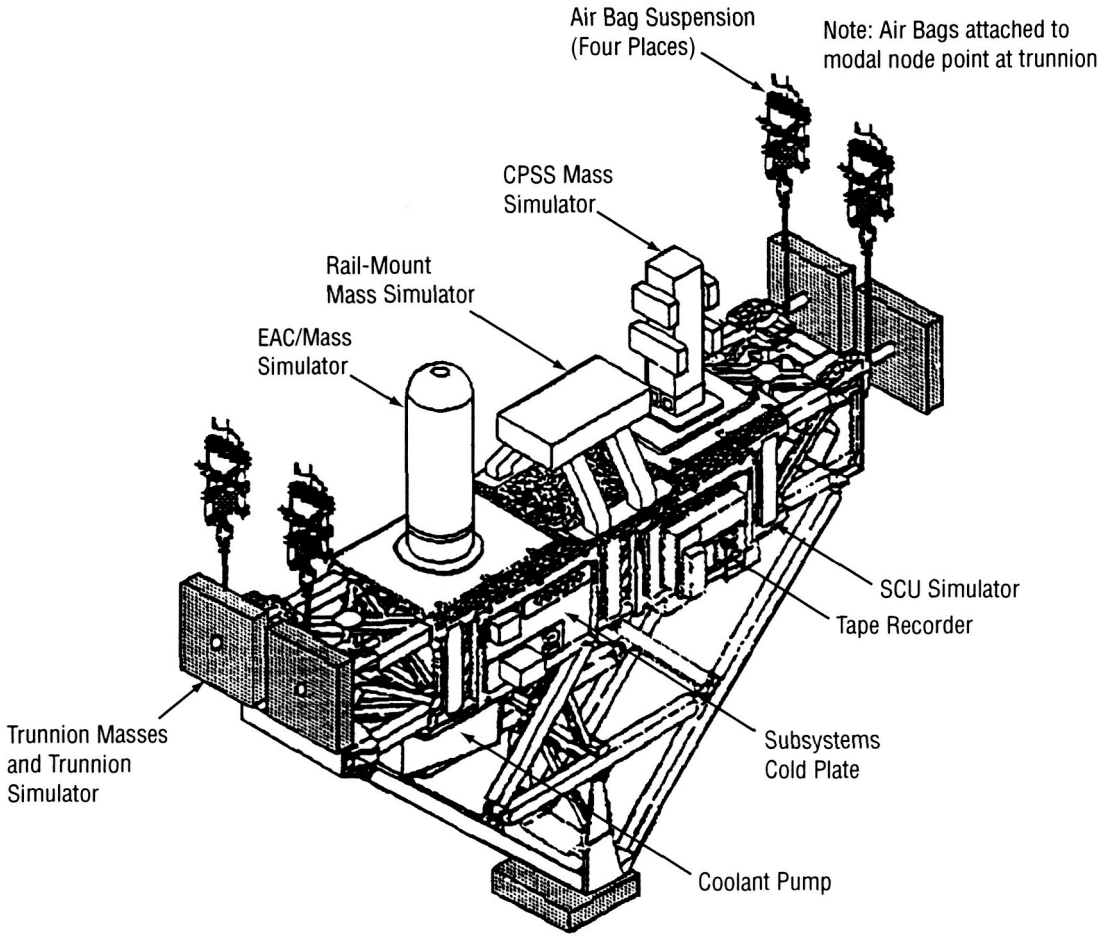

Figure 2. Materials Science Laboratory payload in mass-additive test configuration.

A disadvantage of the mass-additive technique is that, when properly applied in a component mode synthesis approach, many mass-added free-boundary modes are required to derive accurate constrained modes and frequencies. In reference 4, it is shown that for some structures the number of modes required is impractical. Advantages of the method are general ease of performing the measurements in the context of the global modal test and ease of understanding the methodology. Further, it is possible to obtain rotational measurements for the locations where masses are attached to the structure. As shown in figure 2, rectangular masses are typically used in the mass-additive technique. Accelerometers can be attached at the corners and outer edges of the masses to obtain rotational data indirectly, or rotational sensors can be attached at the mass center for direct measurements. If rotational accelerometers are used, more accurate measurements are possible in comparison to non-mass-loaded cases due to the increased amplitudes of the rotational motion. This can be of particular importance for torsional measurements.

1.2 Residual Flexibility Test Method

The concept behind the residual flexibility approach[10] is that a subset of the structure's free-free (unconstrained) mode shapes, along with the residual flexibility of the boundary DOFs, can be used to derive the constrained-boundary modes and frequencies. This can be easily understood for the case of Shuttle payloads, where the interface or boundary DOFs are the translational coordinates of the payload trunnions and keel that are constrained by the orbiter (fig. 1). Residual flexibility of the interfaces provides an approximation of the global free-free modes not measured. Further, it has been shown for simple structures that residual flexibility for a given boundary DOF is simply the flexibility of that boundary. This technique of using an approximation of the effects of neglected higher-order modes, or residual modes, to improve the accuracy of reduced-basis mathematical models was first presented by MacNeal.[11] An improvement of the basic residual approach by including second-order effects, or residual inertia, was presented by Rubin.[12] References 13–27 also present investigations of the residual flexibility approach and related techniques.

Reference 10 describes the application of the residual flexibility approach to the Space Station common module prototype (fig. 3). The general test procedure is as follows: (1) Free-boundary mode shapes and frequencies are obtained in the usual manner by using shakers to excite the structure at the boundary DOFs; (2) modal parameters are then obtained by curve-fitting the resulting responses as functions of frequency over the desired bandwidth; and (3) residual functions, or residual flexibilities, are obtained by subtracting a curve-fitted frequency response function (FRF), which only covers a frequency band of interest, from the full measured FRF, which covers a larger bandwidth. Figure 4 shows two residual functions in acceleration/force format for the common module prototype. For most Shuttle payloads, there are seven of these residual functions to be measured—one for each trunnion/keel translational DOF that is constrained in the orbiter. After the required test data are obtained, the mathematical model of the structure is modified to obtain the best possible agreement with test mode shapes, frequencies, and residual functions. The model is then used in either of two ways: (1) With boundary DOFs analytically constrained to obtain fixed-base modes or (2) with boundary DOFs connected to the orbiter interfaces for coupled Shuttle/payload loads analysis. This general procedure applies for any kind of structure that could be constrained or coupled to other structures in service.

The main drawback using the residual flexibility method is the difficulty in obtaining accurate measurements for the boundary or interface residual functions. Although the functions in figure 4 are clean, they represent average values generated using modal testing software. Most residual measurements are very noisy, making it difficult to identify the residual function. Residual flexibility values are also very small numbers, typically ranging from 1.0E–3 to 1.0E–6 in/lb for translational terms. In addition, the interface FRF must have a well-defined stiffness line (a general upward-sloping trend in acceleration/force format, as evident for higher frequencies in fig. 4) for accurate residual values to be obtainable. The major advantage of this approach is the quick convergence of constrained modes which are derived from free-free modes and residuals, with a reasonably small number of modes.

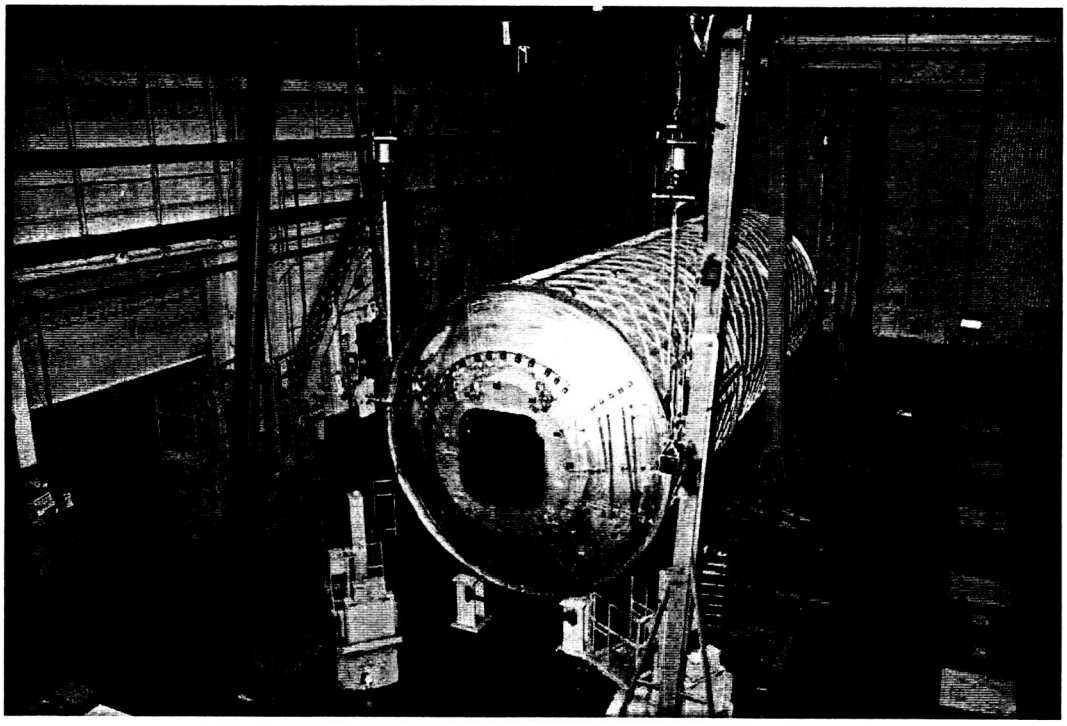

Figure 3. Space Station common module prototype in free-suspension test configuration.

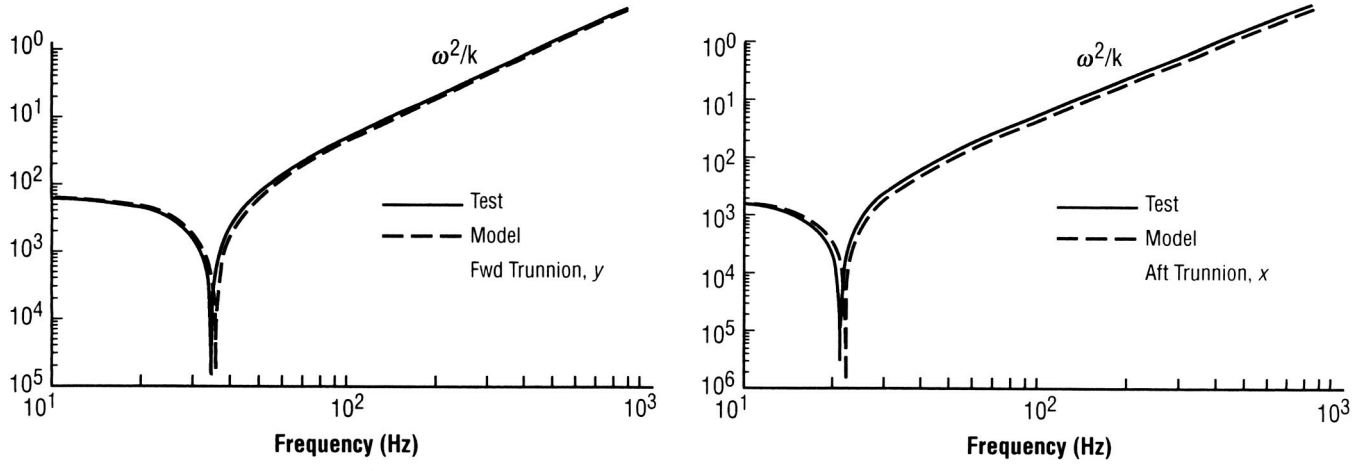

Figure 4. Residual functions for Space Station common module prototype.[17]

2. DEVELOPMENT OF THE HYBRID TEST METHOD

Comparative analysis of the mass-additive and residual flexibility modal test methods described in the previous section shows the following, in summary:

- Residual flexibility approach
  - Major advantage: More accurate in terms of deriving constrained modes from free-suspension data; that is, the convergence rate is higher in the component mode synthesis formulation.
  - Major disadvantages: Difficult to accurately measure residual flexibility values, and rotational data for structure boundaries can only be obtained using expensive rotational sensors.
- Mass-additive technique
  - Major advantages: Very attractive in terms of simplicity of the methodology and general ease of performing measurements; rotational boundary responses can be measured rather easily using translational accelerometers.
  - Major disadvantages: Large number of mass-added modes are required in deriving fixed-boundary modes, making the method impractical for some structures.

Consideration of the advantages and disadvantages of each technique led to the development of a hybrid free-suspension test/analysis approach with more general applicability and flexibility than either of the methods alone. The hybrid formulation is essentially the residual flexibility approach modified to allow mass loading of the structure boundary DOFs for which residual values are to be obtained. Such a formulation overcomes or helps in solving at least three problem areas identified in the comparative analysis:

- Large number of mass-additive modes required for deriving constrained-boundary modes: Overcome because the inclusion of residual flexibility terms with mass-additive modes results in a high rate of convergence for derivation of constrained modes.
- Inability in the residual approach to measure rotations at boundary DOFs: Overcome due to the possibility of attaching translational accelerometers to corners and edges of boundary masses. Viewed a different way, rotational motion is enhanced allowing the possibility of more accurate measurements with rotational sensors if such instrumentation is available.

- Large bandwidth required for measuring residual terms: Large bandwidth required for measuring residual terms is reduced due to presence of boundary masses, which lowers the frequency of local boundary or interface modes.

A hybrid approach of this type should make free-suspension modal test methods applicable to a wider variety of payloads and structures. For example, a Shuttle payload could be considered for testing using the residual flexibility method even though it has interface FRFs exhibiting a large number of modes that effectively hide the stiffness lines. In such a case, the interfaces could be mass loaded to bring each fundamental interface mode to a lower frequency—below some of the modes that mask the stiffness lines. As discussed in the previous section, a characteristic of the mass-additive approach is that interface bending frequencies can be lowered into the frequency bandwidth of the test. The use of mass loading in residual flexibility testing should also make the technique feasible for industrial applications where rotational residual flexibilities may be required. Application of the method for general boundary conditions has been hindered due to difficulties in performing rotational measurements. Reference 7 describes the use of rectangular masses and translational accelerometers to estimate the rotational FRF of a structure. Such an approach, or use of rotational sensors with boundary masses, should allow rotational residual functions to be measured with greater accuracy than in the past.

2.1 Derivation of Governing Equations for Hybrid Method

2.1.1 Development of Hybrid Transformation Matrix

In a hybrid residual flexibility/mass-additive modal test, rectangular masses are attached to boundary or interface DOFs, as shown in figure 2. For this configuration, the undamped equations of motion are written as

$$\left([M]+[\Delta M]\right)\{\ddot{u}\}+[K]\{u\}=\{F(t)\} \tag{1}$$

or

$$[\overline{M}]\{\ddot{u}\}+[K]\{u\}=\{F(t)\} \ , \tag{2}$$

where the mass matrix for the structure with boundary mass loading is $[\overline{M}]=[M]+[\Delta M]$, and $[\Delta M]$ represents the added mass. Free-free elastic and rigid-body modes $[\Phi_n]$ and $[\Phi_R]$ are obtained from an eigensolution of equation (1) for the case $\{F\} = 0$ and are used in subsequent equations discussed in this section. These eigenvectors are referred to as the mass-additive or mass-loaded mode shapes.

Rubin[12] showed that flexible-body displacements for a structure can be written as a first-order approximation of residual effects,

$$\{u_f\}=[G]\{F\}=[A]^T[G_c][A]\{F\} \ , \tag{3}$$

where $[G]$ and $[G_c]$ are the free-free and constrained flexibility matrices, respectively, and for configurations discussed in this TM, apply to the mass-loaded structure. Generally, terms in the equations

presented in this section refer to quantities for the structure with mass-loaded boundaries unless noted otherwise. The flexibility transformation matrix is $[A]=[I]-[\overline{M}][\Phi_R][M_R]^{-1}[\Phi_R]^T$. It is noted that the mode shape matrices in the transformation matrix $[A]$ are the rigid-body modes of the mass-loaded structure (from eigensolution of eq. (1) with $\{F\}=0$), and the generalized mass $[M_R]$ is generated using the rigid-body modes. If the contribution of modes to be retained or measured is removed from the deflection for the flexible structure, the residual flexibility matrix is obtained, as shown in equation (4):

$$\{u_{fr}\}=([G]-[G_n])\{F\}=[G_r]\{F\} \quad . \tag{4}$$

Note that $[G_n] = [\Phi_n][K_n]^{-1}[\Phi_n]^T$ is the flexibility corresponding to the retained or measured elastic mass-additive modes $[\Phi_n]$, and that the generalized stiffness in this expression is based on the retained modes. Equation (4) demonstrates the physical meaning of the residual flexibility $[G_r]$: it is the difference in the full flexibility of the structure and the flexibility based on a set of retained or measured modes. That is, it provides an approximation of mode shapes not retained in a reduced model or not measured in a modal test. If desired, this procedure can be carried a step further to include second-order residual effects,[12] but these will not be shown until later in this TM.

Both MacNeal[11] and Rubin[12] developed a stiffness matrix formulation for component mode synthesis using residual flexibility. Martinez, Carne, and Miller[13] discussed the MacNeal and Rubin representation expressed in a form similar to the Craig-Bampton component synthesis approach.[28] This was a significant step in facilitating practical use of the residual flexibility method, due to wide use of the Craig-Bampton method for model reduction in the aerospace industry. Following the approach of reference 13, but utilizing quantities for boundary DOFs with mass loading, structure displacements can be written in the partitioned form

$$\{u\}=\begin{Bmatrix} u_i \\ u_b \end{Bmatrix}=\begin{bmatrix} \Phi_i & G_{r_{ib}} \\ \Phi_b & G_{r_{bb}} \end{bmatrix}=\begin{Bmatrix} q \\ F_b \end{Bmatrix} , \tag{5}$$

where $[\Phi]$ is the $(N \times n)$ matrix of retained mass-additive modes, and $[G_{r_b}]$ is the boundary partition of the $(N \times N)$ residual flexibility matrix defined in equation (4). Note that N is the size of the original or unreduced model, and n is the number of retained modes. If the lower partition of equation (5) is solved for the boundary forces $\{F_b\}$, and the resulting expression is substituted back in to equation (5), it can be shown that

$$\{u_i\}=\left([\Phi_i]-[G_{r_{ib}}][G_{r_{bb}}]^{-1}[\Phi_b]\right)\{q\}+[G_{r_{ib}}][G_{r_{bb}}]^{-1}\{u_b\} \quad . \tag{6}$$

This form of displacement for the mass-loaded structure results in modified free-free elastic modes (coefficient of $\{q\}$ in eq. (6)) and modified residual attachment modes (coefficient of $\{u_b\}$). Assembly of equation (6) with the identity $\{u_b\} = \{u_b\}$ results in the final expression for displacements of the mass-loaded structure,

$$\begin{Bmatrix} u_i \\ u_b \end{Bmatrix} = \begin{bmatrix} \Phi_i - G_{r_{ib}} G_{r_{bb}}^{-1} \Phi_b & G_{r_{ib}} G_{r_{bb}}^{-1} \\ O & I \end{bmatrix} \begin{Bmatrix} q \\ u_b \end{Bmatrix} = [\overline{T}] \begin{Bmatrix} q \\ u_b \end{Bmatrix} , \tag{7}$$

and the overbar is used in $[\overline{T}]$ to indicate mass-added conditions.

2.1.2 Free-Free Unloaded Model in Terms of Mass-Added Modes and Residuals

In the process of deriving constrained-boundary mode shapes and frequencies from a free-free mass-added model, it is first necessary to express the equations of motion for the free-free structure with unloaded boundaries in terms of mass-additive modes and residual flexibility. This step is essential since constraining the boundary DOFs without first analytically removing the masses would yield incorrect results in most cases. For example, for a structural model of a Shuttle payload that has only certain translational boundary DOFs constrained in flight, the unconstrained mass-loaded DOF would experience undesired inertia loading influencing the mode shapes and frequencies.

The unloading process is accomplished by subtracting the added mass terms, $[\Delta M]$, from equation (2), yielding an alternate expression for the model without boundary masses,

$$\left([\overline{M}] - [\Delta M] \right) \{\ddot{u}\} = [K]\{u\} = \{F(t)\} , \tag{8}$$

which can also be written in partitioned form:

$$\left(\begin{bmatrix} M_{ii} + \Delta M_{ii} & M_{ib} + \Delta M_{ib} \\ M_{bi} + \Delta M_{bi} & M_{bb} + \Delta M_{bb} \end{bmatrix} - \begin{bmatrix} \Delta M_{ii} & \Delta M_{ib} \\ \Delta M_{bi} & \Delta M_{bb} \end{bmatrix} \right) \begin{Bmatrix} \ddot{u}_i \\ \ddot{u}_b \end{Bmatrix} + \begin{bmatrix} K_{ii} & K_{ib} \\ K_{bi} & K_{bb} \end{bmatrix} \begin{Bmatrix} u_i \\ u_b \end{Bmatrix} = \begin{Bmatrix} 0 \\ F_b \end{Bmatrix} . \tag{9}$$

In equation (9), the mass addition affects all six DOFs at an attachment point, with the possibility arising that a boundary mass can load interior DOFs, and not just the DOFs partitioned to the matrix boundary. The implications of this are discussed further later in this section. The partitioned form of the residual flexibility matrix corresponding to equation (9) is given by

$$[G_r] = \begin{bmatrix} G_{r_{ii}} & G_{r_{ib}} \\ G_{r_{bi}} & G_{r_{bb}} \end{bmatrix} . \tag{10}$$

Substitution of equation (7) into equation (8) allows the equations of motion to be written in terms of generalized coordinates and physical boundary coordinates:

$$\left(\left[\overline{M}\right]-\left[\Delta M\right]\right)\left[\overline{T}\right]\begin{Bmatrix}\ddot{q}\\ \ddot{u}_b\end{Bmatrix}+\left[K\right]\left[\overline{T}\right]\begin{Bmatrix}q\\ u_b\end{Bmatrix}=\begin{Bmatrix}0\\ F_b\end{Bmatrix} . \tag{11}$$

Premultiplication of equation (11) by $[\overline{T}]^T$ yields the desired reduced model with unloaded boundary DOFs in terms of mass-additive modes and residual flexibility,

$$\left\{\left[\overline{T}\right]^T\left[\overline{M}\right]\left[\overline{T}\right]-\left[\overline{T}\right]^T\left[\Delta M\right]\left[\overline{T}\right]\right\}\begin{Bmatrix}\ddot{q}\\ \ddot{u}_b\end{Bmatrix}+\left[\overline{T}\right]^T\left[K\right]\left[\overline{T}\right]\begin{Bmatrix}q\\ u_b\end{Bmatrix}=\left[\overline{T}\right]^T\begin{Bmatrix}O\\ F_b\end{Bmatrix} , \tag{12}$$

which can be written in the form

$$\left\{\left[\overline{\overline{M}}\right]-\left[\overline{T}\right]^T\left[\Delta M\right]\left[\overline{T}\right]\right\}\begin{Bmatrix}\ddot{q}\\ \ddot{u}_b\end{Bmatrix}+\left[\overline{\overline{K}}\right]\begin{Bmatrix}q\\ u_b\end{Bmatrix}=\left[\overline{T}\right]^T\begin{Bmatrix}O\\ F_b\end{Bmatrix} , \tag{13}$$

where $\left[\overline{\overline{M}}\right]=\left[\overline{T}\right]^T\left[\overline{M}\right]\left[\overline{T}\right]$ and $\left[\overline{\overline{K}}\right]=\left[\overline{T}\right]^T\left[K\right]\left[\overline{T}\right]$. For mass-additive modes normalized to unit modal mass, it can be shown using the approach of reference 13 that

$$\left[\overline{\overline{M}}\right]=\begin{bmatrix}I_{nn}+\Phi_{nb}^T J_{bb}\Phi_{nb} & -\Phi_{nb}^T J_{bb}\\ \text{sym.} & J_{bb}\end{bmatrix}$$

$$\left[\overline{\overline{K}}\right]=\begin{bmatrix}\Omega_{nn}^2+\Phi_{nb}^T G_{r_{bb}}^{-1}\Phi_{nb} & -\Phi_{nb}^T G_{r_{bb}}^{-1}\\ \text{sym.} & G_{r_{bb}}^{-1}\end{bmatrix} , \tag{14}$$

where Ω_{nn} is the diagonal matrix of retained frequencies ω_n, and Φ_{nb} is the boundary partition of the retained modes. Also in equation (14), $\left[J_{bb}\right]=\left[G_{r_{bb}}\right]^{-1}\left[H_{bb}\right]\left[G_{r_{bb}}\right]^{-1}$ and $\left[H_{bb}\right]=\left[G_{r_b}\right]^T\left[\overline{M}\right]\left[G_{r_b}\right]$, where $\left[G_{r_b}\right]$ contains the two partitions of the residual flexibility matrix shown in equation (5). The second-order residual effects for the mass-loaded configuration, or residual inertia effects, are contained in $[H_{bb}]$. The mass and stiffness matrices in equation (14) represent the full-residual or Rubin method, with only residual damping effects neglected. If the residual inertia effects are neglected in equation (14), the MacNeal formulation is obtained and the generalized mass matrix for the structure

with mass-loaded boundaries, $[\overline{\overline{M}}]$, becomes the identity matrix. Neglecting residual inertia is a commonly used approximation to simplify the technique.[13,14] In subsequent references to mode shapes in this TM, it is understood that retained modes are under discussion, and the *n* subscript is dropped.

2.1.2.1 Development of the Generalized Added-Mass Matrix. It remains to evaluate the generalized added mass term in equation (13). Use of the transformation defined in equation (7) with $[\Delta M]$ from equation (9) yields the following expression:

$$[\overline{T}]^T[\Delta M][\overline{T}]=[\overline{\Delta M}]=\begin{bmatrix}\Phi_i-G_{r_{ib}}G_{r_{bb}}^{-1}\Phi_b & G_{r_{ib}}G_{r_{bb}}^{-1}\\ 0 & I\end{bmatrix}^T\begin{bmatrix}\Delta M_{ii} & \Delta M_{ib}\\ \Delta M_{bi} & \Delta M_{bb}\end{bmatrix}\begin{bmatrix}\Phi_i-G_{r_{ib}}G_{r_{bb}}^{-1}\Phi_b & G_{r_{ib}}G_{r_{bb}}^{-1}\\ 0 & I\end{bmatrix}, \tag{15}$$

which can also be written in the form

$$[\overline{T}]^T[\Delta M][\overline{T}]=[\overline{\Delta M}]=\begin{bmatrix}\overline{\Delta M}_{ii} & \overline{\Delta M}_{ib}\\ \overline{\Delta M}_{bi} & \overline{\Delta M}_{bb}\end{bmatrix}, \tag{16}$$

where

$$[\overline{\Delta M}_{ii}]=\left[\left(\Phi_i^T-\Phi_b^T G_{r_{bb}}^{-1}G_{r_{ib}}^T\right)\Delta M_{ii}\left(\Phi_i-G_{r_{ib}}G_{r_{bb}}^{-1}\Phi_b\right)\right] \tag{17}$$

$$[\overline{\Delta M}_{ib}]=\left[\left(\Phi_i^T-\Phi_b^T G_{r_{bb}}^{-1}G_{r_{ib}}^T\right)\left(\Delta M_{ii}G_{r_{ib}}G_{r_{bb}}^{-1}+\Delta M_{ib}\right)\right] \tag{18}$$

$$[\overline{\Delta M}_{bi}]=\left[\left(G_{r_{bb}}^{-1}G_{r_{ib}}^T\Delta M_{ii}+\Delta M_{bi}\right)\left(\Phi_i-G_{r_{ib}}G_{r_{bb}}^{-1}\Phi_b\right)\right] \tag{19}$$

$$[\overline{\Delta M}_{bb}]=\left[\left(G_{r_{bb}}^{-1}G_{r_{ib}}^T\Delta M_{ii}+\Delta M_{bi}\right)G_{r_{ib}}G_{r_{bb}}^{-1}+G_{r_{bb}}^{-1}G_{r_{ib}}^T\Delta M_{ib}+\Delta M_{bb}\right]. \tag{20}$$

These equations for the generalized added-mass matrix are for the general case where only a portion of the DOFs at a given mass attachment point are to be constrained or coupled to another structure, which is the case for Shuttle payloads. The implication of this is that some of the interior DOFs have mass loading, as can be seen in equations (17)–(20). For the case where all six DOFs at each mass attachment point are constrained or used in coupling, the problem is greatly simplified, since all mass-loaded DOFs are partitioned to the matrix boundaries, and $[\Delta M_{ii}] = [\Delta M_{ib}] = [\Delta M_{bi}] = 0$. In the case where no interior DOFs are mass loaded, it can be seen from equations (17)–(20) that the generalized added-mass matrix reduces to

$$\left[\overline{\Delta M}\right]=\begin{bmatrix}0 & 0\\ & \\ 0 & \Delta M_{bb}\end{bmatrix}. \tag{21}$$

Also for equation (21), $[\Delta M_{bb}]$ has dimensions $(n_b \times n_b)$, where $n_b = 6\, n_m$, and n_m is the number of boundary masses. It should be noted that in the context of this discussion, interior DOFs can include part of the mass attach point DOF, such as rotational coordinates. The term interior does not imply that the DOFs are actually on the physical interior of the structure, far removed from the physical boundaries, but rather that the DOFs have been partitioned in the mathematical model to the interior of the matrices.

Although equations (17)–(20) are very useful for seeing the effects of constraining or coupling all six DOFs at each mass attach point versus using only a portion of the mass attach point DOFs, they do not show which added-mass terms correspond to residual inertia. This is important because generally the residual inertia terms are not utilized due to difficulty in accurately measuring them, and the MacNeal formulation is used. In order to observe which terms in equation (16) (or eqs. (17)–(20)) are residual inertia effects, it is necessary to perform the transformation shown in equation (15) in two steps. As shown in reference 13, the transformation defined in equation (7) can be written as the product of two transformation matrices,

$$\left[\overline{T}\right]=\left[\overline{T_1}\right]\left[\overline{T_2}\right]=\begin{bmatrix}\Phi_i & G_{r_{ib}}\\ & \\ \Phi_b & G_{r_{bb}}\end{bmatrix}\begin{bmatrix}I & 0\\ & \\ -G_{r_{bb}}^{-1}\Phi_b & G_{r_{bb}}^{-1}\end{bmatrix}, \tag{22}$$

where $\left[\overline{T_1}\right]$ is given in equation (5), and $\left[\overline{T_2}\right]$ is the transformation that allows the elimination of boundary forces in going from equation (5) to equation (7).

If the transformation of the equations of motion for the structure with unloaded boundaries, equation (8), is done in two steps using $\left[\overline{T_1}\right]$ and $\left[\overline{T_2}\right]$ separately, the following expression is obtained:

$$\left[\overline{T_2}\right]^T\left[\overline{T_1}\right]^T\left\{\left[\overline{M}\right]-\left[\Delta M\right]\right\}\left[\overline{T_1}\right]\left[\overline{T_2}\right]\begin{Bmatrix}\ddot{q}\\ \\ \ddot{u}_b\end{Bmatrix}+\left[\overline{T_2}\right]^T\left[\overline{T_1}\right]^T\left[K\right]\left[\overline{T_1}\right]\left[\overline{T_2}\right]\begin{Bmatrix}q\\ \\ u_b\end{Bmatrix}=\left[\overline{T_2}\right]^T\left[\overline{T_1}\right]^T\left\{F(t)\right\}. \tag{23}$$

The resulting transformed mass and stiffness, $\left[\overline{\overline{M}}\right]$ and $\left[\overline{\overline{K}}\right]$, respectivley, are identical to equation (14), but the transformed added-mass matrix $\left[\overline{\Delta M}\right]$ shown in equations (24)–(28) looks different than equations (16)–(20) because the original added-mass matrix $[\Delta M]$ appears in full form without partitioning:

$$\left[\overline{T_2}\right]^T\left[\overline{T_1}\right]^T[\Delta M]\left[\overline{T_1}\right]\left[\overline{T_2}\right]=\left[\overline{\Delta M}\right]=\begin{bmatrix}\overline{\Delta M_{ii}} & \overline{\Delta M_{ib}}\\ \overline{\Delta M_{bi}} & \overline{\Delta M_{bb}}\end{bmatrix}, \tag{24}$$

where

$$\left[\overline{\Delta M_{ii}}\right]=\left[\Phi^T\Delta M\Phi-\Phi_b^T G_{r_{bb}}^{-1}G_{r_b}^T\Delta M\Phi-\Phi^T\Delta M G_{r_b}G_{r_{bb}}^{-1}\Phi_b+\Phi_b^T G_{r_{bb}}^{-1}G_{r_b}^T\Delta M G_{r_b}G_{r_{bb}}^{-1}\Phi_b\right] \tag{25}$$

$$\left[\overline{\Delta M_{ib}}\right]=\left[\Phi^T\Delta M G_{r_b}G_{r_{bb}}^{-1}-\Phi_b^T G_{r_{bb}}^{-1}G_{r_b}^T\Delta M G_{r_b}G_{r_{bb}}^{-1}\right] \tag{26}$$

$$\left[\overline{\Delta M_{bi}}\right]=\left[G_{r_{bb}}^{-1}G_{r_b}^T\Delta M\Phi-G_{r_{bb}}^{-1}G_{r_b}^T\Delta M G_{r_b}G_{r_{bb}}^{-1}\Phi_b\right] \tag{27}$$

$$\left[\overline{\Delta M}_{bb}\right]=\left[G_{r_{bb}}^{-1}G_{r_b}^T\Delta M G_{r_b}G_{r_{bb}}^{-1}\right]. \tag{28}$$

Analogous to the discussion following equation (14) and similar to an approach discussed in references 12–14, the residual added inertia effects can be found in equations (25)–(28). Defining $[\Delta J_{bb}]=\left[G_{r_{bb}}\right]^{-1}[\Delta H_{bb}]\left[G_{r_{bb}}\right]^{-1}$, where $[\Delta H_{bb}]=\left[G_{r_b}\right]^T[\Delta M]\left[G_{r_b}\right]$, it can be seen that the second-order residual effects for the added-mass matrix, $|\Delta M|$, are contained in $|\Delta H_{bb}|$ just as the residual inertia effects for the mass-loaded configuration are contained in $|H_{bb}|$. Using the expressions for $|\Delta H_{bb}|$ and $|\Delta J_{bb}|$, equations (25)–(28) can be written in more compact form:

$$\left[\overline{\Delta M_{ii}}\right]=\left[\Phi^T\Delta M\Phi-\Phi_b^T G_{r_{bb}}^{-1}G_{r_b}^T\Delta M\Phi-\Phi^T\Delta M G_{r_b}G_{r_{bb}}^{-1}\Phi_b+\Phi_b^T\Delta J_{bb}\Phi_b\right] \tag{29}$$

$$\left[\overline{\Delta M_{ib}}\right]=\left[\Phi^T\Delta M G_{r_b}G_{r_{bb}}^{-1}-\Phi_b^T\Delta J_{bb}\right] \tag{30}$$

$$\left[\overline{\Delta M_{bi}}\right]=\left[G_{r_{bb}}^{-1}G_{r_b}^T\Delta M\Phi-\Delta J_{bb}\Phi_b\right] \tag{31}$$

$$\left[\overline{\Delta M_{bb}}\right]=\left[\Delta J_{bb}\right]. \tag{32}$$

2.1.2.2 Equations of Motion in Terms of Mass-Added Modes and Residuals. Equations (29)–(32), along with equations (12)–(14), define the hybrid method for the general case where not all mass attach points are to be constrained or coupled to another structure, and mass addition can occur for

interior terms of the mass matrix. Both residual flexibility and residual inertia effects are also included at this stage. Repeating equation (13) as equation (33) and utilizing equations (29)–(32) for $\left[\overline{\Delta M}\right]$ results in the following general formulation for the free-free unloaded model equations of motion in terms of mass-additive modes and residuals:

$$\left\{\left[\overline{\overline{M}}\right]-\left[\overline{\Delta M}\right]\right\}\begin{Bmatrix}\ddot{q}\\ \ddot{u}_b\end{Bmatrix}+\left[\overline{\overline{K}}\right]\begin{Bmatrix}q\\ u_b\end{Bmatrix}=\left[\overline{T}\right]^T\begin{Bmatrix}0\\ F_b\end{Bmatrix}, \tag{33}$$

where

$$\left[\overline{\overline{M}}\right]-\left[\overline{\Delta M}\right]=$$

$$\begin{bmatrix} I-\Phi^T\Delta M\Phi+\Phi_b^T G_{r_{bb}}^{-1}G_{r_b}^T\Delta M\Phi+\Phi^T\Delta M G_{r_b}G_{r_{bb}}^{-1}\Phi_b+\Phi_b^T(J_{bb}-\Delta J_{bb})\Phi_b & -\Phi_b^T(J_{bb}-\Delta J_{bb})-\Phi^T\Delta M G_{r_b}G_{r_{bb}}^{-1} \\ -(J_{bb}-\Delta J_{bb})\Phi_b-G_{r_{bb}}^{-1}G_{r_b}\Delta M\Phi & J_{bb}-\Delta J_{bb} \end{bmatrix} \tag{34}$$

and the generalized stiffness is unchanged from equation (14),

$$\left[\overline{\overline{K}}\right]=\begin{bmatrix}\Omega^2+\Phi_b^T G_{r_{bb}}^{-1}\Phi_b & -\Phi_b^T G_{r_{bb}}^{-1}\\ \text{sym.} & G_{r_{bb}}^{-1}\end{bmatrix}. \tag{35}$$

The general hybrid method formulation given in equations (33)–(35), which corresponds to the Rubin method, can be simplified considerably if the residual inertia effects corresponding to $[\overline{M}]$ and $[\Delta M]$, which are $[J_{bb}]$ and $[\Delta J_{bb}]$, respectively, are neglected. In that case,

$$\left[\overline{\overline{M}}\right]-\left[\overline{\Delta M}\right]=\begin{bmatrix} I-\Phi^T\Delta M\Phi+\Phi_b^T G_{r_{bb}}^{-1}G_{r_b}^T\Delta M\Phi+\Phi^T\Delta M G_{r_b}G_{r_{bb}}^{-1}\Phi_b & -\Phi^T\Delta M G_{r_b}G_{r_{bb}}^{-1} \\ -G_{r_{bb}}^{-1}G_{r_b}\Delta M\Phi & 0 \end{bmatrix} \tag{36}$$

which corresponds to the MacNeal approach. The generalized stiffness is unchanged and is given by equation (35).

Finally, for the case where all six DOFs at each mass attachment points are to be constrained or coupled to another structure, and all mass-loaded DOFs are partitioned to the matrix boundary, the formulation is simplified further. In that case, the transformed added-mass matrix $\left[\overline{\Delta M}\right]$ is given by equation (21), and the transformed mass for the unloaded model in terms of mass-additive modes and full residuals is given by

$$\left[\overline{\overline{M}}\right]-\left[\overline{\Delta M}\right]=\begin{bmatrix} I+\Phi_b^T J_{bb}\Phi_b & -\Phi_b^T J_{bb} \\ -J_{bb}\Phi_b & J_{bb}-\Delta M_{bb} \end{bmatrix}, \tag{37}$$

which differs only in the boundary partition from the basic Rubin formulation with no mass loading. If residual inertia is neglected in equation (37), the transformed mass matrix for the unloaded model becomes

$$\left[\overline{\overline{M}}\right]-\left[\overline{\Delta M}\right]=\begin{bmatrix} I & 0 \\ 0 & 0 \end{bmatrix}. \tag{38}$$

Neglecting $[\Delta M_{bb}]$ is justified on the basis of equations (20), (28), and (32), which show that $\left[\Delta J_{bb}\right]=\left[\Delta M_{bb}\right]$ for the case of mass loading limited to boundary DOFs. Further, $[\Delta M_{bb}]$ is small in comparison to the diagonal terms of the identity matrix in equation (38). An alternative formulation neglecting $[J_{bb}]$ in equation (37) but retaining $[\Delta M_{bb}]$ could also be investigated. Numerical results for this case were not investigated in the context of the current study. In either case described in equations (37) and (38) for mass loading limited to boundary DOFs, the generalized stiffness is unchanged and is defined in equation (35).

2.1.3 Constrained Unloaded Model in Terms of Mass-Added Modes and Residuals

The reduced hybrid model defined by equation (33) is the form used for coupling to other structures or components. For cases where it is desired to derive fixed-boundary modes and frequencies, another step remains in the analysis. Starting with the most general formulation given by equations (33)–(35), the hybrid reduced model with constrained boundaries is obtained by setting boundary displacements to zero and striking all matrix rows and columns with boundary terms. This operation results in the following expression:

$$\left[\left(\overline{\overline{M}}-\overline{\Delta M}\right)_{nn}\right]\{\ddot{q}\}+\left[\overline{\overline{K}}_{nn}\right]\{q\}=\{0\}, \tag{39}$$

where for use of full residuals and mass loading possible for interior and boundary DOFs, the generalized mass matrix is, from equation (34),

$$\left[\left(\overline{\overline{M}}-\overline{\Delta M}\right)_{nn}\right]=\left[I-\Phi^T\Delta M\Phi+\Phi_b^T G^{-1}_{r_{bb}} G^T_{r_b}\Delta M\Phi+\Phi^T\Delta M G_{r_b} G^{-1}_{r_{bb}}\Phi_b+\Phi_b^T(J_{bb}-\Delta J_{bb})\Phi_b\right] \tag{40}$$

and the generalized stiffness is given by

$$\left[\overline{\overline{K}}_{nn}\right]=\left[\Omega^2+\Phi_b^T G_{r_{bb}}^{-1}\Phi_b\right] . \tag{41}$$

If residual inertia is neglected, the constrained-boundary generalized mass reduces to

$$\left[\left(\overline{\overline{M}}-\overline{\Delta M}\right)_{nn}\right]=\left[I-\Phi^T\Delta M\Phi+\Phi_b^T G_{r_{bb}}^{-1}G_{r_b}^T\Delta M\Phi+\Phi^T\Delta M G_{r_b}G_{r_{bb}}^{-1}\Phi_b\right] . \tag{42}$$

For the case of mass loading limited to boundary DOFs, but including full residuals, the constrained-boundary generalized mass becomes

$$\left[\left(\overline{\overline{M}}-\overline{\Delta M}\right)_{nn}\right]=\left[I+\Phi_b^T J_{bb}\Phi_b\right] . \tag{43}$$

Further, if residual inertia is neglected, the generalized mass becomes the identity matrix. In all of these cases, the constrained-boundary generalized stiffness is unchanged and given by equation (41).

Interestingly, equation (43) has the same form as the constrained-boundary generalized mass matrix for the basic Rubin method with no mass loading. However, it must be kept in mind that the mode shapes shown in equation (43) are mass-additive modes, so the effect of mass loading does appear upon the dynamics of the structure. The observation that no ΔM terms appear in equation (43) does point out an interesting fact, however. If mass loading is limited to boundary DOFs, that is, DOFs partitioned to the matrix boundary, it is not necessary to analytically remove the added mass before constraining the model. However, as shown in equations (40) and (42), if mass loading of interior DOFs occurs, the added mass must be removed before constraining the model. If the model is to be used for substructuring and coupling to other components, the added mass must always be analytically removed before the coupling is done.

The frequencies obtained from eigensolution of equation (39) are the constrained frequencies of interest. However, to obtain physical constrained-boundary mode shapes, a back-transformation of the modes obtained in the eigensolution of equation (39), $[\Phi_{nn}]$, must be done. This is accomplished by using the transformation matrix defined in equation (7) and forming the following matrix equation for constrained physical modes,

$$\left[\Phi_c\right]=\left[\overline{T}\right]\begin{bmatrix}\Phi_{nn}\\ \\ 0\end{bmatrix} . \tag{44}$$

Zeros must be added in the last n_b rows of the free-free mode shape matrix to make it compatible with $\left[\overline{T}\right]$, since n_b DOFs were eliminated by constraining the boundaries in equation (39).

2.2 Frequency Response Formulation of Hybrid Method

The hybrid matrix equations of motion developed in the preceding sections are extremely useful for pretest analysis to determine which residual terms are needed and how many mode shapes are required in dynamic testing of the mass-loaded test article. If it is desired to develop a test-verified constrained model, these equations allow convergence studies to determine if a selected number of mode shapes and residual terms is sufficient for obtaining accurate constrained modes and frequencies. However, when it comes to experimental implementation of the hybrid method, an FRF formulation is more practical because test residual functions and mode shapes are obtained from measured FRFs. Further, it can be seen from the matrix formulation in equation (4) that computation of residual flexibility requires the full flexibility (inverted stiffness) matrix. Obviously, the full flexibility matrix is not available experimentally.

By developing a frequency response formulation, a practical implementation for developing a test-verified model involves the following: (1) Comparison of free-free modes for model and test, with appropriate model updates; (2) comparison of measured and predicted boundary FRFs and residual functions (obtained from FRFs), with model updates as required; and (3) constraining of the model boundary DOFs or coupling to another structural component. The response function equations are discussed in the following paragraphs.

As described by Rubin in reference 12, displacement can be written as a function of frequency,

$$[U(\omega)] = [Y(\omega)]\{\mathbf{F}(\omega)\} , \tag{45}$$

where $[Y]$ is the displacement/force FRF matrix and $\{\mathbf{F}\}$ is the applied force vector, both as functions of frequency. However, it must be noted that in contrast to reference 12, all terms in equation (45) and following equations in this section refer to the mass-loaded structure. The residual FRF matrix, or residual function matrix as it will be designated here, is obtained by subtracting from the full FRFs in equation (45) the modal FRFs containing rigid-body and elastic free-free modes that are to be measured or retained. The undamped modal FRF matrix is given by

$$[Y_m(\omega)] = -[\Phi_R]1/\omega^2[M_R]^{-1}[\Phi_R]^T + [\Phi_n][\Lambda_n]^{-1}[M_n]^{-1}[\Phi_n]^T , \tag{46}$$

where $[M_n]$ is the generalized mass associated with the measured or retained modes $|\Phi_n|$, and $[\Lambda_n|$ is the diagonal matrix $\left[\omega_n^2 - \omega^2\right]$. The residual function matrix becomes

$$[Y_r(\omega)] = [Y(\omega)] - [Y_m(\omega)] , \tag{47}$$

which can be approximated over the frequency range of interest by the undamped form,

$$[Y_r(\omega)] = [G_r] + \omega^2[H_r] , \tag{48}$$

corresponding to the residual flexibility matrix given by equation (4). The residual inertia matrix in equation (48) is given by $[H_r]=[G_r]^T[\overline{M}][G_r]$. For comparison of residual flexibility values, the undamped forms of equations (46)–(48) should be sufficient. However, if analytical and test FRF results are being compared, inclusion of damping may be desirable in some instances. In that case, $[\Lambda_n]=\left[\omega_n^2+i2\zeta_n\omega\omega_n-\omega^2\right]$ in equation (46) and the residual function takes the form

$$[Y_r(\omega)]=[G_r]+\omega^2[H_r]-i\omega[B_r] \ , \tag{49}$$

where $[B_r]$ is the residual damping matrix.

For practical computations, residual functions are obtained individually as functions of frequency rather than in matrix form. Residual flexibility for a particular residual function is the value of the function at zero frequency, as can be easily seen from equations (48) and (49). Each value of $[G_r]$ obtained in this manner is equal to the corresponding value from equations (4) and (10).

It is noted that the second-order term $[H_r]$ in equations (48) and (49), the residual inertia, was only used in this TM for obtaining smooth curve fits of residual functions. Residual inertia was not included in reduced models or in the model correlation work described in subsequent sections. In section 2.3, the curve-fitting procedure for estimating residual flexibility values from experimental residual functions is described.

2.3 Statistical Least-Squares Curve-Fitting Procedure for Identification of Experimental Residual Flexibility Values

As will be shown later in this TM, noisy frequency response and residual test data are often observed at low frequencies, particularly in antiresonance regions of the FRF. In addition, undesired peaks or spikes generally occur in experimental residual functions at system resonances. These spikes are observed due to inaccuracies in approximating damping in the synthesized FRF, which are generated using system identification software in modal testing. Because of these effects, a second-order polynomial curve fit of experimental residual functions is required to determine the residual flexibility (constant coefficient) and the residual inertia (second-order coefficient) shown in equations (48) and (49). The procedure for determining experimental residual terms is presented for the damped form of the residual function, equation (49), for generality. The approach presented in this section is the curve-fitting method developed by Bookout,[22] and also used by Tinker and Bookout.[23] First, it can be seen that the residual function appears in the general complex form $\mathbf{a}+i\mathbf{b}$. This general form can be equated to equation (49),

$$\boldsymbol{a}+i\mathbf{b}=[G_r]+\omega^2[H_r]-i\omega[B_r] \ , \tag{50}$$

and like terms can be separated to yield

$$[B_r]=-\mathbf{b}/\omega \tag{51}$$

directly from the imaginary term. Real terms are given by

$$\mathbf{a}=[G_r]+\omega^2[H_r] \tag{52}$$

and must be determined by curve fitting. The least-squares conditions are obtained by expressing equation (52) in matrix coefficient form,

$$\mathbf{a}=[R][X] \tag{53}$$

where

$$[R]=\begin{bmatrix}1 & \omega^2\end{bmatrix} \tag{54}$$

and

$$[X]=\begin{bmatrix}G_r \\ \\ H_r\end{bmatrix} . \tag{55}$$

The residual flexibility and residual inertia terms are then obtained as

$$[X]=[R]^{-1}\mathbf{a} \ . \tag{56}$$

These residual values are compared to analytical residuals in the test/model correlation process.

A theoretical residual function in displacement/force format is relatively flat at low frequencies and has slight upward curvature at higher frequencies. Variations of consecutive values of the residual function should therefore be small. When examining the residual functions produced from test data, these characteristics can be seen in an overall sense. However, in regions of poor or noisy data, consecutive residual values can have large variations in magnitude. It is apparent that a weighting function is needed that applies low weighting to data points having large variation with respect to neighboring points and high weighting to data in regions of small variations.

The required weighting function can be expressed statistically in terms of sample variance, where each sample consists of two or more neighboring data points. Since the variance represents the amount of variation between data points in the sample, regions of the residual function with high variation (containing spikes and noise) can be given low weight by defining the weighting function as the inverse of the sample variance,

$$W(j)=\frac{1}{s^2}=\frac{p-1}{\sum_{i=1}^{p}(x_i-\bar{x})^2} \quad j=1,\ldots,k-p+1 \ , \tag{57}$$

where s^2 is the sample variance, k is the total number of data points, p is the number of data points in the sample, and $\bar{x}$ is the mean of the sample.[22]

Premultiplying both sides of equation (53) by the weighting function W gives

$$W\mathbf{a}=W[R][X] \ . \tag{58}$$

Next, premultiplying both sides of equation (58) by $[R]^T$ and solving for $[X]$ results in the final form of the residual flexibility and residual inertia terms,

$$[X]=\left([R]^T W[R]\right)^{-1}[R]^T W\,\mathbf{a} \ . \tag{59}$$

In this form, there is no need to normalize the weighting function W.

By stepping through the test data, the variance of each data point with respect to the neighboring points can be calculated. The weighting value for each data point is set equal to the inverse of the variance assigned to that data point. This gives the desired effect that, when the variances of neighboring data points are high, the weighting function value is low, and vise versa. Incorporating the weighting function of equation (57) into the least-squares curve fit allows determination of smooth experimental residual functions having the characteristics previously described for theoretical displacement/force functions.

In previous studies, different weighting matrices generated by examining samples with two, three, and four data points were used in the curve fit process. The error range for the residual flexibility term produced by examining different sample sizes was found to vary considerably, with best results achieved using three data points. Based on these earlier findings, sample sizes of three data points were used in the curve fitting described in this TM. In addition, the frequency range of curve-fitted data was varied to determine the effect on accuracy of the residual flexibility value. This was done because experimental residual functions typically are very noisy at low frequencies. Further description of the statistically weighted curve-fitting procedure is given in reference 22.

3. ANALYTICAL APPLICATION OF HYBRID METHOD TO SHUTTLE PAYLOAD SIMULATOR

A simple Shuttle payload simulator was designed specifically for studies of free-suspension modal test techniques. This payload simulator has frequency content somewhat similar to real payloads, with a number of well-spaced global mode shapes, and it also has prominent flexible interfaces (simulating Shuttle payload trunnions which interface with the orbiter). This structure, shown in figures 5–7, was also designed to be simple enough that high confidence could be obtained for the model through correlation to free-free test data. Dimensions of the beam-like interfaces (trunnions) were chosen to provide prominent stiffness lines, or well-defined linear regions in the frequency responses at higher frequencies, for enhancing the measurement of residual flexibility values.

Initially, the basic residual flexibility method,[10] based on equation (14) but with no mass loading of the trunnion interfaces, was applied to the payload simulator. However, the procedures are the same when mass loading of the boundaries is utilized; such mass loading is discussed later in this section. The procedure followed in this approach was to (1) measure a set of free-free modes and frequencies using shaker excitation (fig. 6); (2) measure the acceleration/force frequency response functions in X, Y, Z directions at the ends of all four trunnions (fig. 7), this time using impact hammer excitation; (3) modify the model in a global sense to obtain the best possible agreement with test frequencies and mode shapes, (4) modify the model in the trunnion regions to match the experimental response functions in both the minima (antiresonances) and maxima (peaks or resonances); and (5) compare the measured and predicted residual flexibility functions and values. It is noted that normally a 5-percent frequency error or less is the goal for such model correlation activities, but in this case a 1-percent goal was established so that insight could also be gained into accuracy of residual measurements. In addition, hammer impact excitation was used for the small, lightweight trunnions because it was believed that connecting a shaker to them would unacceptably modify their dynamic behavior.

3.1 Correlation of Free-Boundary Mode Shapes and Frequencies

The procedures for mode shape correlation have little difference for residual flexibility and hybrid method testing compared to any free-suspension test. It should be noted, however, that a higher number of modes may need to be measured and used in model correlation than for a standard free-free test. Also, it is possible that the frequency errors should be lower than the standard 5-percent limit currently used in model correlation. These potential differences, which are still in the process of being fully verified and quantified, are due to the synthesis process described in the previous section of this TM, where the free-suspension modes and boundary residual flexibility values are used to derive constrained-boundary modes.

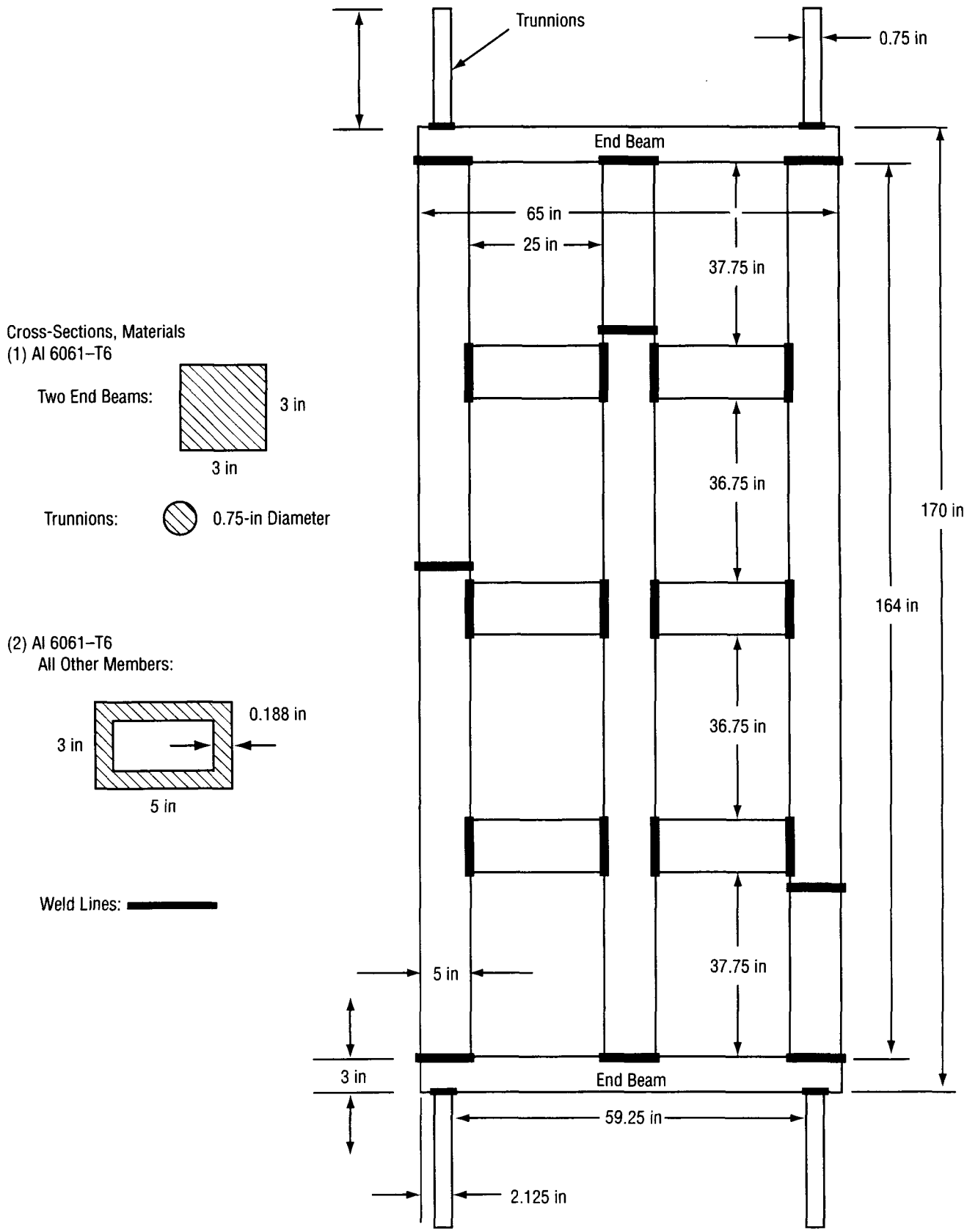

Figure 5. Space Shuttle payload simulator structure.

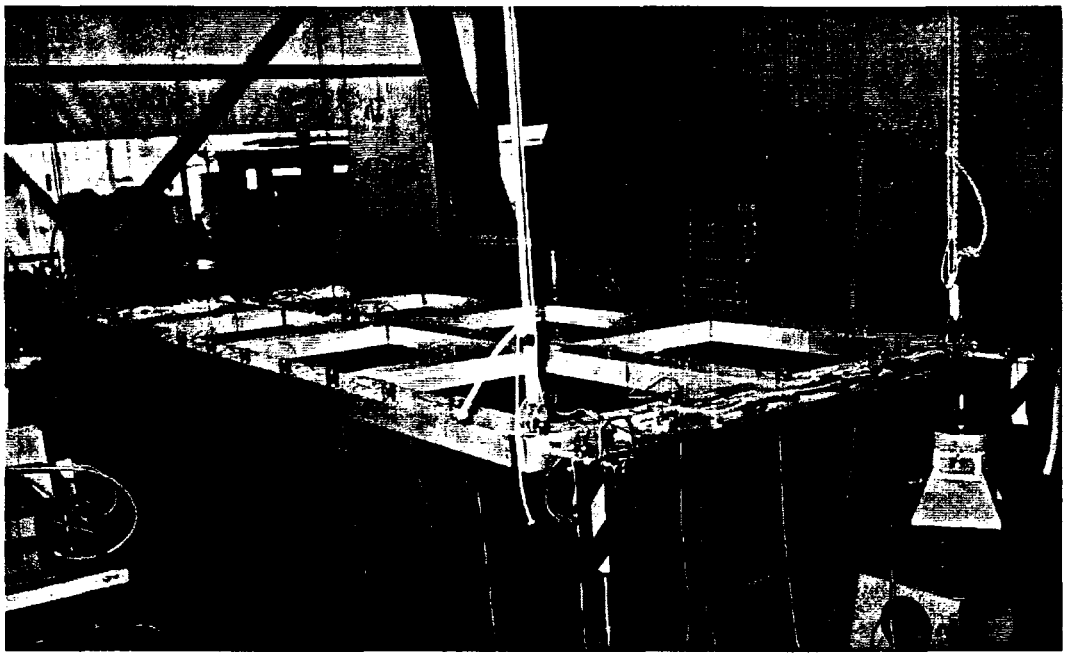

Figure 6. Shuttle payload simulator in free-suspension modal test configuration.

Figure 7. Trunnion interface region of payload simulator.

To correlate the model to the measured modal data, the analyst compares the predicted and measured frequencies and mode shapes to identify errors in geometry, material properties, and modeling assumptions. These comparisons are done based on engineering judgment, either alone or in combination with the use of analytical tools, to find errors and shortcomings in the model. In the cases described in this TM, the mode shape correlations were done based on engineering judgment and visual inspection of the modes. For the payload simulator, the welded intersections of the hollow box beams comprising the model (fig. 5) were found to be the critical areas for global model updating. This was due to the nature of the welds—they were outer surface welds, having widely varying stiffness from one weld to another and having lower stiffness than the box beam cross sections. Beam elements were used to model the welds, and a trial-and-error approach was used to find proper material and geometric properties. Table 1 contains the first 10 test/analysis frequency comparisons and mode shape orthogonalities after model correlation. For this simple structure, it was possible to obtain frequency errors of 1 percent or less.

Table 1. Comparison of test and analytical free-free modes for payload simulator, after model correlation (zero mass loading).

Mode Number	Test Frequency	Analytical Frequency	Percent Error	*X* Orthog. Diagonal
1	16.56	16.52	0.28	0.99498
2	21.21	21.29	–0.37	0.99469
3	46.49	46.10	0.86	0.99384
4	51.40	51.57	–0.33	0.99003
5	75.73	75.33	0.52	0.99905
6	83.80	84.32	–0.62	0.99015
7	96.78	96.11	0.70	0.98078
8	98.68	98.37	0.32	0.99246
9	105.72	105.98	–0.24	0.98155
10	112.87	113.03	–0.14	0.98598
11	135.70	136.02	–0.25	0.94888
12	136.70	137.79	–0.80	0.93058
13	138.70	139.39	–0.50	0.99716
14	167.36	167.41	–0.03	0.98405

3.2 Model Updating for Boundary Frequency Response

Using initial test data for drive point FRF at one of the trunnion simulators, a large discrepancy was observed between the predicted and measured antiresonance frequency (at the function minimum). Parameter studies were performed to identify modifications to the model that would improve the agreement. It was found that drastic, unreasonable changes in geometry and material properties of the trunnion still did not produce acceptable agreement with the measured data. Finally, additional measurements were taken to determine if errors existed in the test data. It was found that by using various impact

hammer tips of different hardnesses, the measured antiresonance frequency shifted by several hertz. Use of the softest tip available provided the data considered most accurate. This is explained by the fact that soft tips provide more energy at lower frequencies, while hard tips excite higher frequencies of the structure. It is also quite difficult in general to measure clean antiresonances in FRFs due to the very low response amplitudes in the vicinity of a function minimum. Antiresonance response amplitudes with hammer excitation can be near the "noise floor" or response limit of the accelerometers.

After more accurate frequency response measurements had been obtained, model correlation for the trunnion regions of the payload simulator was done. By varying the trunnion stiffness (modulus or area moments of inertia), the antiresonance frequencies were shifted to obtain the best possible agreement with test. The problem encountered in this process is that when good antiresonance agreement was obtained, the FRF peaks did not agree well. In the test configuration, a considerable amount of lumped mass was present on each trunnion due to accelerometers at the midpoints and ends, tape, adhesive, and wires connected to the accelerometers. By varying the amount of mass lumped at the center and end of each trunnion in the model, it was found that the FRF peaks and stiffness lines could be shifted to provide better agreement with measured data. A justification for the final net increase in lumped mass on each trunnion is the fact that the wires, adhesive, and tape were initially ignored in the model. It can be seen in figure 8 that excellent agreement was finally obtained between the test and model trunnion interface FRFs.

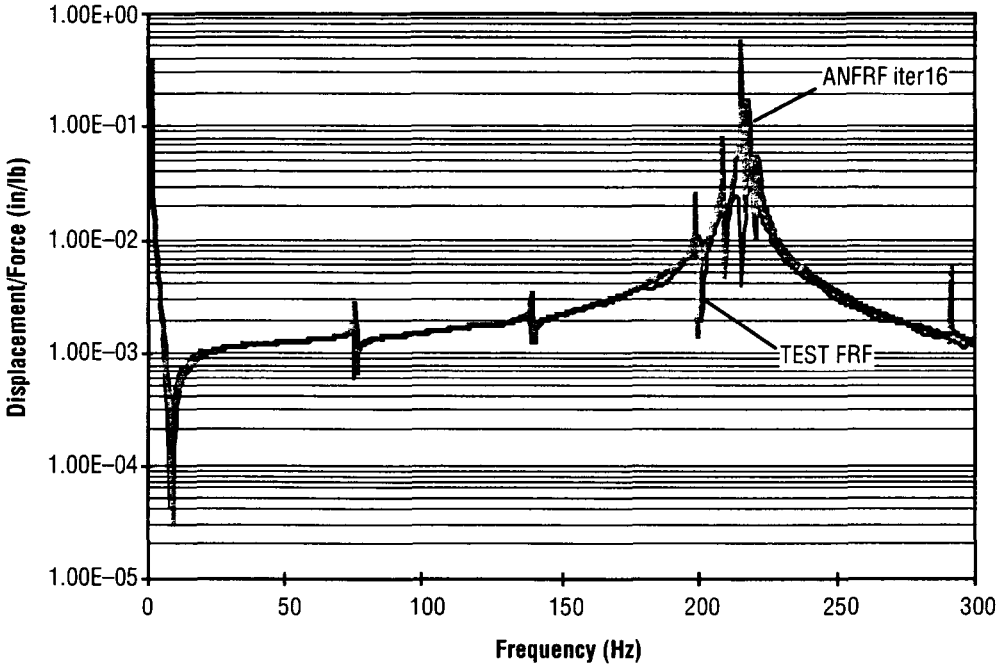

Figure 8. Test/analysis trunnion response functions, after model updates (zero mass loading).

3.3 Comparison of Residual Flexibility Values for Boundary Degrees of Freedom

The next step in the process was to compare the boundary residual flexibility values from test and the model that had been correlated to both the global free-free modes and trunnion response data. As discussed previously, residual functions, which are obtained by subtracting interface FRFs based

on the measured modes from full measured interface FRFs, are typically very noisy. To obtain accurate estimates of measured residual flexibility, the statistical least-squares curve-fitting approach described in a previous section was used.[22] This curve-fitting technique provides an estimate of both residual flexibility and residual inertia. However, only the residual flexibility values were used in model correlation. Initially, the percent error was not as low as desired (within a few percent of test), so the trunnion stiffness and mass properties were further modified as described in the previous section to obtain acceptable correlation. As a note of interest, in error analysis for the Materials Science Laboratory, the Shuttle payload structure in figure 2 showed that up to 10–15 percent error in the residual values can be present and still yield constrained frequencies within 5 percent error. However, for this simple payload simulator, higher accuracy was desired.

Table 2 compares the analytical residual values (both before and after final model correlation to FRF data) and test results for each trunnion in the *X*, *Y*, and *Z* directions. It is noted that the *X* direction was along the main axis of each trunnion, while *Y* and *Z* were both bending directions. Excellent agreement with test (near 2 percent error and below) was obtained for all eight residual flexibility values in bending directions, but poor agreement was obtained for the axial direction. This is a problem that will not likely be overcome in hybrid and residual flexibility testing of Shuttle payload-type structures in the near future due to several reasons, including the following: (1) Dominant stiffness lines are not observed in trunnion axial-direction data, making the curve-fitting process for test data generally inaccurate; (2) the residual flexibility values are even smaller for the axial direction than for bending; and (3) the trunnion axial FRF test data are typically very noisy, which, when combined with the approximations in modal parameter estimation, yields very noisy residual functions that are difficult to interpret. Fortunately for Shuttle payloads, inaccurate axial-direction residuals for trunnions is not an issue since such payloads are only constrained in bending directions of the trunnions and keel. At this point, the analytical model with zero mass loading had been correlated with test as well as could be done.

Table 2. Residual flexibility values for Shuttle payload simulator, before and after model updates to trunnions (zero mass loading, 14 free-free modes).

Model Location	Test Residuals, (in/lb)	Analytical Residuals Before Updates (in/lb)	Initial Percent Error	Analytical Residuals After Updates (in/lb)	Final Percent Error
51*X*	1.1597E–05 *	4.8099E–06	---------	4.7566E–06	---------
Y	1.2277E–03	1.3852E–03	12.83	1.2420E–03	1.16
Z	1.2853E–03	1.4049E–03	9.31	1.2611E–03	–1.88
53*X*	1.7254E–05 *	4.9603E–06	---------	4.9068E–06	---------
Y	1.2335E–03	1.3856E–03	12.33	1.2424E–03	0.72
Z	1.2784E–03	1.4051E–03	9.91	1.2614E–03	–1.33
55*X*	--------- *	4.8318E–06	---------	4.7784E–06	---------
Y	1.2368E–03	1.4083E–03	13.87	1.2635E–03	2.16
Z	1.3057E–03	1.4269E–03	9.28	1.2815E–03	–1.85
57*X*	1.0012E–05 *	4.7943E–06	---------	4.7410E–06	---------
Y	1.2359E–03	1.3632E–03	10.30	1.2216E–03	–1.16
Z	1.2250E–03	1.3830E–03	12.90	1.2408E–03	1.29

* Confidence in experimental residual flexibility values for the *X*–direction is low because stiffness lines are not present in the response functions and curve-fitting breaks down. These directions are unimportant for Shuttle payloads.

3.4 Use of Payload Simulator Model for Hybrid Method Parameter Studies

Investigation of the equations presented in this TM has been done through parameter studies using the payload simulator model. For these parameter studies, the model had been updated to agree with measured free-free modes and frequencies but had not been correlated with trunnion interface response functions and residual flexibility values. However, as shown in table 2, percent error between model and test residual values was under 14 percent for the trunnion bending directions, which for some cases is within the error bounds identified in the Materials Science Laboratory error analysis mentioned in the previous section. Further, the parameter studies were mainly comparative in nature for (1) different boundary mass configurations, (2) different residual terms, and (3) different numbers of mode shapes, so that the partially correlated model was sufficiently accurate for the objectives of the studies. It is noted that for the parameter studies described in this section, rectangular masses were added symmetrically to all four trunnions of the payload simulator model.

3.4.1 Hybrid Method With Full Residuals (Modified Rubin Method)

Initially the payload simulator model was used for investigations of the hybrid Rubin method, which includes both residual flexibility and residual inertia, along with mass loading of the structure boundaries. This is the most general technique described in this TM, as stated previously, though not necessarily the most practical for test implementation, due to the requirement of measuring residual inertia effects. These second-order effects are very small, and differences between test and model can be greater than one or two orders of magnitude.

For all the hybrid/Rubin method cases discussed, 20 mass-additive mode shapes, including 6 rigid-body modes, were retained in the modal synthesis. In the first cases studied, all 6 DOFs at the end of each payload simulator trunnion (fig. 5), a total of 24 DOFs, were placed in the boundary partitions of the matrices in the equations of motion, equations (33)–(35). As discussed in section 2.1.2.1, near equation (21), mass loading is limited to the boundary DOFs in this case, since all mass loaded DOFs are to be constrained. Three different mass loading conditions were evaluated: (1) Zero mass loading reference case, (2) 0.5 lb attached to each trunnion, and (3) 5-lb masses on each trunnion.

In table 3, derived constrained frequencies and mode shape cross-orthogonality values are compared for the unloaded, 0.5-lb mass, and 5-lb mass loading conditions. As stated in the previous paragraph, 24 boundary DOFs were constrained in each case, and 20 free-free mass-additive modes were used. With the exception of mode 15 for the unloaded case, all derived frequencies are nearly exact, with errors below 0.1 percent, and the diagonal orthogonality values are near 1. It can be seen from table 3 that considerably more constrained-boundary modes could be derived for the zero mass loading case compared to either of the loaded-boundary cases. This is due to the fact that the added boundary masses lowered the bending frequencies of the trunnions, with the result that in the selected sets of 20 modes there were fewer global modes and more localized trunnion modes than for the unloaded case. A thorough pretest analysis must always be done when using boundary mass loading to determine the best mass properties for a given structure and test configuration. This will assure that the desired constrained modes are derived from the measured or retained mass-additive modes.

Table 3. Effect of different boundary mass loadings on derived constrained frequencies and mode orthogonality for hybrid Rubin method (24 boundary DOFs, 20 modes).

Exact Frequency	Derived Frequency (0 lb)	X Orthog. Diagonal (0 lb)	Derived Frequency (0.5 lb)	X Orthog. Diagonal (0.5 lb)	Derived Frequency (5 lb)	X Orthog. Diagonal (5 lb)
9.2768	9.2768	1.0000	9.2768	1.0000	9.2768	1.0000
18.7627	18.7627	1.0000	18.7627	1.0000	18.7627	1.0000
20.6366	20.6366	1.0000	20.6366	1.0000	20.6366	1.0000
23.9799	23.9800	1.0000	23.9800	1.0000	23.9800	1.0000
32.8235	32.8236	1.0000	32.8247	1.0000	32.8235	1.0000
40.7146	40.7146	1.0000	40.7146	1.0000	40.7503	1.0000
40.8733	40.8734	1.0000	40.8734	1.0000	40.8733	1.0000
56.3890	56.3896	1.0000	56.3900	1.0000	56.3893	1.0000
60.0858	60.0862	1.0000	60.0861	1.0000	60.0861	1.0000
79.8798	79.8810	1.0000	79.8814	1.0000		
91.6779	91.6815	1.0000	91.6869	1.0000		
96.6930	96.6936	1.0000	96.7022	0.9999		
107.9900	107.9949	1.0000				
116.7489	116.7606	1.0000				
126.1755	129.1603	0.9964				
138.8683	138.8816	0.9999				
141.6920	141.7253	0.9991				
142.5079	142.5607	0.9990				

It was also desirable to observe the effects of having mass loading of interior DOFs; i.e., cases where not all DOFs affected by the added masses are to be constrained. This more general case was investigated for the hybrid Rubin method by constraining only translations at the end of each trunnion (12 DOFs total) for the payload simulator. Results are shown in table 4 for 0.5-lb mass loading at each trunnion and 20 modes retained. Of course, the constrained frequencies are generally lower than for the six-DOF-constrained cases, but no loss in accuracy of derived modes is seen when mass loading of interior DOFs occurs. Again, the derived modes and frequencies are almost exact when both residual flexibility and residual inertia are included.

These results point out the great accuracy achievable for reduced models and derived constrained modes using the hybrid full residual or Rubin approach. However, the disadvantage of the method is the difficulty of measuring residual inertia as stated earlier in this section. For this reason, the hybrid residual flexibility method, or hybrid MacNeal formulation, will be emphasized for the remainder of this TM. However, estimates of residual inertia are required when curve-fitting experimental residual functions to obtain residual flexibility values.

Table 4. Derived constrained modes for hybrid Rubin method (0.5-lb mass, 12 boundary DOFs, 20 modes).

Exact Frequency (Hz)	Derived Frequency (Hz)	X Orthog. Diagonal
6.9501	6.9501	1.0000
9.6823	9.6823	1.0000
12.4921	12.4921	1.0000
13.7879	13.7879	1.0000
22.8302	22.8302	1.0000
28.6450	28.6450	1.0000
34.1967	34.1968	1.0000
50.5303	50.5305	1.0000
53.6326	53.6330	1.0000
77.4622	77.4636	1.0000
87.1822	87.1881	1.0000
96.2350	96.2400	0.9999

3.4.2 Hybrid Residual Flexibility Technique (Modified MacNeal Approach)

Due to the great practical importance of the hybrid residual flexibility formulation for experimental implementation, the effects of the following variables were investigated in a highly detailed parameter study: (1) Size and weight of added masses, (2) number of retained mass-additive modes, (3) residual flexibility terms retained, and (4) number of constrained DOFs. In addition, results for basic residual flexibility method with no mass loading and for basic mass-additive approach with no residual terms were obtained as reference cases for (1) and (3).

The studies are broken down into two broad categories:

(1) Six DOFs constrained at each mass attach point (24 DOFs total), described by equations (33), (35), and (38)

(2) Three DOFs constrained at each mass attach point (translations only, total 12 DOFs), governed by equations (33) and (35)–(36).

Convergence characteristics of the derived constrained modes for these two configurations are described in the following sections.

3.4.2.1 Results for Six Degrees of Freedom Constrained at Each Mass Attach Point. The first parameter to be discussed, weight of added masses, was investigated for three cases: (1) No mass loading, (2) 0.5-lb masses, and (3) 5-lb masses. Of course, the case for no mass loading represents the basic residual flexibility approach. Table 5 shows a comparison of derived constrained frequencies and mode cross-orthogonalities (with exact modes) for the three mass loading cases, using 20 retained mass-additive modes and full residual flexibility matrices for all cases in the reduced mass and stiffness matrices. The residual flexibility matrices referred to here can be seen in equations (7) and (35). In all three boundary mass configurations, accurate constrained modes were obtained, though the 5-lb case

Table 5. Comparison of derived constrained modes for hybrid MacNeal method with different mass loadings (20 mass-additive modes, full residual flexibility matrix, 24 boundary DOFs).

Exact Frequency	Derived Frequency (0 lb)	X Orthog. Diagonal (0 lb)	Derived Frequency (0.5 lb)	X Orthog. Diagonal (0.5 lb)	Derived Frequency (5 lb)	X Orthog. Diagonal (5 lb)
9.2768	9.2774	1.0000	9.2773	1.0000	9.2774	1.0000
18.7627	18.7836	1.0000	18.7754	1.0000	18.7648	1.0000
20.6366	20.6493	1.0000	20.6415	1.0000	20.6410	1.0000
23.9799	24.0117	1.0000	23.9865	1.0000	24.0000	1.0000
32.8235	32.9330	1.0000	32.8794	1.0000	32.8812	1.0000
40.7146	40.8183	1.0000	40.7687	1.0000	42.7748	1.0000
40.8733	41.3649	1.0000	41.3134	1.0000	41.4633	0.9998
56.3890	56.5504	1.0000	56.4205	1.0000	56.4502	1.0000
60.0858	60.4672	1.0000	60.2583	0.9999	60.1910	0.9999
79.8798	80.1406	1.0000	80.3566	1.0000		
91.6779	92.7889	0.9987	95.5041	0.9914		
96.6930	96.7142	1.0000	96.7356	0.9926		
107.9900	108.3370	0.9997				
116.7489	117.2540	0.9997				
126.1755	148.4911	0.9907				
138.8683	139.4997	0.9919				
141.6920	143.7859	0.9718				
142.5079	144.9400	0.9709				

was less accurate and fewer modes could be derived. This occurred because the retained set of 20 mass-additive modes had more localized trunnion modes and fewer global structure modes than the cases for zero and 0.5-lb mass loading. These results point out the importance of pretest analysis and selecting a proper mass size and weight that will allow the desired number of constrained modes to be derived with accuracy. Of the mass loading configurations presented here for the Shuttle payload simulator, the 0.5-lb case is more desirable. Though more modes could be derived with no mass loading, the rotations at the trunnions, particularly torsion, cannot be accurately measured without boundary masses.

Investigation of the second parameter, number of retained mass-additive modes, is described next. Again, the full residual flexibility matrices that appear in equations (7) and (35) were utilized. In tables 6–8, derived constrained frequencies are shown with mode shape cross-orthogonality for the 0.5-lb, 5-lb, and zero mass loading cases, respectively. Each table lists the derived constrained modes for 10, 15, and 20 retained mass-additive modes. In each mass loading case, the progress of convergence of the constrained modes can clearly be seen as a function of the number of retained mass-additive modes. All three mass loading cases start out with the same number (7) of derived modes and have comparable accuracy, though the 5-lb case lags behind the other cases slightly. The zero added-mass case and 0.5-lb case both increased to 12 derived constrained modes for 15 retained mass-additive modes, while the 5-lb case shows no increase in the number of derived modes. However, the accuracy of the constrained frequencies did increase significantly for the 5-lb case in going from 10 to 15 retained mass-additive modes. A similar situation is seen for the 0.5-lb mass loading case when going from 15 to 20 retained mass-additive modes.

Table 6. Effect of retained mass-added modes on derived constrained modes for hybrid MacNeal method (0.5-lb loading, full residual flexibility, 24 boundary DOFs).

Exact Frequency	10 Mass-Added Modes		15 Mass-Added Modes		20 Mass-Added Modes	
	Derived Frequency	*X* Orthog. Diagonal	Derived Frequency	*X* Orthog. Diagonal	Derived Frequency	*X* Orthog. Diagonal
9.2768	9.2779	1.0000	9.2774	1.0000	9.2773	1.0000
18.7627	18.8367	1.0000	18.7823	1.0000	18.7754	1.0000
20.6366	20.6532	1.0000	20.6531	1.0000	20.6415	1.0000
23.9799	24.0514	1.0000	24.0369	1.0000	23.9865	1.0000
32.8235	33.0968	1.0000	32.9077	1.0000	32.8794	1.0000
40.7146	42.8722	1.0000	40.7955	1.0000	40.7687	1.0000
40.8733	42.1046	0.9993	41.3294	1.0000	41.3134	1.0000
56.3890			56.7825	0.9997	56.4205	1.0000
60.0858			60.9173	0.9999	60.2583	0.9999
79.8798			80.7216	1.0000	80.3566	1.0000
91.6779			96.9188	0.9946	95.5041	0.9914
96.6930			97.4750	0.9943	96.7356	0.9926

Table 7. Effect of retained mass-added modes on derived constrained modes for hybrid MacNeal method (5-lb loading, full residual flexibility, 24 boundary DOFs).

Exact Frequency	10 Modes		15 Modes		20 Modes	
	Derived Frequency	*X* Orthog. Diagonal	Derived Frequency	*X* Orthog. Diagonal	Derived Frequency	*X* Orthog. Diagonal
9.2768	9.2776	1.0000	9.2774	1.0000	9.2774	1.0000
18.7627	18.8727	1.0000	18.8314	1.0000	18.7648	1.0000
20.6366	20.9275	0.9997	20.7148	1.0000	20.6410	1.0000
23.9799	24.7170	0.9992	24.0459	0.9999	24.0000	1.0000
32.8235	34.0192	0.9999	32.9186	0.9998	32.8812	1.0000
40.7146	43.2223	1.0000	43.0194	0.9999	42.7748	1.0000
40.8733	44.6197	0.9968	41.6791	0.9982	41.4633	0.9998
56.3890					56.4502	1.0000
60.0858					60.1910	0.9999

Table 8. Effect of retained mass-added modes on derived constrained modes for hybrid MacNeal method (zero mass loading, full residual flexibility, 24 boundary DOFs).

	10 Modes		15 Modes		20 Modes	
Exact Frequency	Derived Frequency	X Orthog. Diagonal	Derived Frequency	X Orthog. Diagonal	Derived Frequency	X Orthog. Diagonal
9.2768	9.2780	1.0000	9.2777	1.0000	9.2774	1.0000
18.7627	18.8362	1.0000	18.7836	1.0000	18.7836	1.0000
20.6366	20.6564	1.0000	20.6564	1.0000	20.6493	1.0000
23.9799	24.0546	1.0000	24.0546	1.0000	24.0117	1.0000
32.8235	33.0833	1.0000	33.0045	1.0000	32.9330	1.0000
40.7146	42.8673	1.0000	40.8184	1.0000	40.8183	1.0000
40.8733	42.0271	0.9994	41.3650	1.0000	41.3649	1.0000
56.3890			56.7381	0.9998	56.5504	1.0000
60.0858			60.6858	0.9999	60.4672	1.0000
79.8798			80.1407	1.0000	80.1406	1.0000
91.6779			92.7893	0.9987	92.7889	0.9987
96.6930			96.7575	0.9997	96.7142	1.0000
107.9900					108.3370	0.9997
116.7489					117.2540	0.9997
126.1755					148.4911	0.9907
138.8683					139.4997	0.9919
141.6920					143.7859	0.9718
142.5079					144.9400	0.9709

The conclusion to be drawn from tables 6–8 is that the 5-lb mass loading case performs worse than the other cases because the masses are too heavy for the payload simulator structure. The 0.5-lb case performs very well in comparison. However, if there is no need to measure rotations, and the boundary FRFs and residual functions are satisfactory in the desired bandwidth, mass loading should not be utilized. The basic residual flexibility method should be used in such cases because more constrained modes can be derived using a given number of free-free modes in the synthesis process.

The third parameter investigated was the number of residual flexibility terms retained in the reduced stiffness matrix, as shown in equation (35). Note that the reduced mass matrix in equation (38) has no residual flexibility terms. It is desirable to reduce the number of residual flexibility terms in the formulation if possible, in order to reduce the number of measurements required for experimental implementation. Previous investigations have shown that the diagonal terms of $\left[G_{r_{bb}}\right]$ are much easier to measure with accuracy than the off-diagonal terms. It is noted that these parameter studies apply only to the reduced stiffness matrix. The transformation matrix in equation (44) was used with full $\left[G_{r_{bb}}\right]$ and $\left[G_{r_{ib}}\right]$ for all cases.

Initially, for the 24 boundary DOF cases, only the diagonal values of $\left[G_{r_{bb}}\right]$ were used, but it was found that a fairly large number of mass-additive modes (25–30) were required for acceptable accuracy of derived constrained modes. It can be difficult to develop a test-correlated model that accurately represents that many mode shapes. For comparison to these results, the full $\left[G_{r_{bb}}\right]$ matrix was used in equation (35). This was found to work very well, even for small numbers of mass-additive modes,

and representative results are shown in table 9 for the 0.5-lb mass loading case, where 20 mass-additive modes (14 elastic) were retained. Derived constrained modes in table 9 are compared for diagonal $[G_{r_{bb}}]$ and full $[G_{r_{bb}}]$ in equation (35). The disadvantage of using the full $[G_{r_{bb}}]$ matrix is that it may be impossible to verify the off-diagonal terms experimentally; measurement of the diagonal terms is much easier, as stated in the previous paragraph. Engineering judgment is required in determining whether to use only the diagonal terms of $[G_{r_{bb}}]$ with a larger set of mass-additive modes.

Table 9. Effect of retained residual terms on derived constrained modes in hybrid MacNeal method (0.5-lb loading, 20 mass-added modes, 24 boundary DOFs).

	Diagonal $[G_{r_{bb}}]$		Full $[G_{r_{bb}}]$	
Exact Frequency	Derived Frequency	*X* Orthog. Diagonal	Derived Frequency	*X* Orthog. Diagonal
9.2768	7.9465	0.9777	9.2773	1.0000
18.7627	16.0974	0.9922	18.7754	1.0000
20.6366	15.7103	0.9679	20.6415	1.0000
23.9799	16.3415	0.9300	23.9865	1.0000
32.8235	26.1688	0.9503	32.8794	1.0000
40.7146	37.6595	0.9909	40.7687	1.0000
40.8733	34.2264	0.9908	41.3134	1.0000
56.3890	54.0115	0.9776	56.4205	1.0000
60.0858	53.1553	0.8987	60.2583	0.9999
79.8798	82.7598	0.9762	80.3566	1.0000
91.6779	103.3862	0.8857	95.5041	0.9914
96.6930	96.4199	0.9967	96.7356	0.9926

3.4.2.2 Results for Three Degrees of Freedom Constrained at Each Mass Attach Point. Similar studies to those described in the previous section were done for the Shuttle payload simulator with only translations to be constrained at each boundary mass attachment location (12 DOFs constrained total). Mass loading of 0.5 lb at each trunnion was utilized, and a zero mass loading case was analyzed for comparison. Similar to the case for six DOFs constrained at each mass attach point, these parameter studies apply to the reduced mass and stiffness matrices only. For the transformation matrix in equation (44), the full $[G_{r_{bb}}]$ and $[G_{r_{ib}}]$ partitions were used in all cases.

For the case of full residual flexibility terms in the reduced mass and stiffness matrices, a pattern similar to that shown in table 6 for convergence of derived constrained modes was observed. Constrained frequency errors were very low in comparison to exact results. Further, there was virtually no loss in accuracy when neglecting $[G_{r_{ib}}]$ and using only the full $[G_{r_{bb}}]$ residuals in the reduced mass and stiffness matrices, equations (35)–(36). Again, the frequency errors were very low. However, when the residual flexibility terms were reduced to only the diagonals of $[G_{r_{bb}}]$, a clear loss in accuracy of derived constrained modes was observed. This is seen in table 10, where results are shown for derived constrained modes when retaining 10, 15, and 25 mass-additive modes. As stated in the previous

section, it can be difficult to correlate a model to test data for 25 modes. However, accuracy of constrained modes for 20 retained mass-additive modes (not shown in table 10) was actually worse than for 15 retained modes, showing that up to 25 modes could be required.

Table 10. Derived constrained modes for different numbers of mass-added modes in hybrid MacNeal method, with only diagonal $\left[G_{r_{bb}}\right]$ residual terms (0.5-lb loading, 12 boundary DOFs).

Exact Frequency	10 Modes		15 Modes		25 Modes	
	Derived Frequency	*X* Orthog. Diagonal	Derived Frequency	*X* Orthog. Diagonal	Derived Frequency	*X* Orthog. Diagonal
6.9501	7.0181	1.0000	6.5489	0.9969	6.9476	1.0000
9.6823	9.7548	1.0000	9.3592	0.9998	9.6728	1.0000
12.4921	12.2298	1.0000	13.9098	0.8735	12.5757	1.0000
13.7879	13.7778	1.0000	14.0869	0.8714	13.7871	1.0000
22.8302	23.1873	1.0000	21.7631	0.9900	22.8220	1.0000
28.6450	29.0594	1.0000	29.1923	0.9952	28.6230	1.0000
34.1967	52.4894	1.0000	32.5939	0.9991	33.7316	0.9991
50.5303	50.5625	1.0000	53.5009	0.9931	50.6110	0.9998
53.6326			54.1238	0.9994	53.6327	1.0000
77.4622			77.7251	0.9996	77.5186	1.0000
87.1822			93.2500	0.9788	87.1747	1.0000
96.2350			97.0181	0.9859	96.2351	1.0000
107.1969					107.1979	1.0000
114.3559					114.3576	1.0000
126.1380					166.0426	0.9287
137.9789					238.5921	0.2929
138.7379					138.7391	0.9990

Table 10 also shows that use of 15 retained mass-additive modes gave worse results for derived constrained modes than the case for 10 retained modes. These results show that there were modes in the larger set that did not contribute to the constrained-boundary configuration, and actually hurt convergence. This also points out the potential value of selecting mass-additive modes that contribute most to the constrained-boundary modes through use of modal participation calculations. However, such an analysis is not included in the context of this TM.

For comparison to the 0.5-lb mass-loaded configuration, analysis was done for the 12-DOF-constrained model using the basic MacNeal or residual flexibility approach with zero mass loading of the boundaries. Table 11 shows the convergence characteristics of derived constrained modes for use of 10, 15, and 20 retained mass-additive modes, where only diagonal $\left[G_{r_{bb}}\right]$ residuals were utilized. The results of table 11 compared to table 10 point out clearly that use of mass loading in the residual flexibility approach can result in slower convergence of constrained modes, or alternatively, require additional residual flexibility terms. As stated previously, if rotations are not to be constrained and the boundary FRFs and residual functions are satisfactory for obtaining residual flexibility values, mass loading should not be used, and either the basic residual flexibility method or basic Rubin method should be used.

Table 11. Derived constrained modes for different numbers of mass-added modes in hybrid MacNeal method, with only diagonal $\left[G_{r_{bb}}\right]$ residual terms (zero mass loading, 12 boundary DOFs).

	10 Modes		15 Modes		20 Modes	
Exact Frequency	Derived Frequency	X Orthog. Diagonal	Derived Frequency	X Orthog. Diagonal	Derived Frequency	X Orthog. Diagonal
6.9501	6.9780	1.0000	6.9673	1.0000	6.9614	1.0000
9.6823	9.7726	1.0000	9.6470	1.0000	9.6709	1.0000
12.4921	12.3795	1.0000	12.5119	1.0000	12.5165	1.0000
13.7879	13.8117	1.0000	13.9772	1.0000	13.6573	1.0000
22.8302	23.0062	1.0000	22.9567	1.0000	22.9258	1.0000
28.6450	28.9372	1.0000	28.5938	1.0000	28.9203	1.0000
34.1967	53.2095	1.0000	33.4080	0.9998	33.3839	0.9998
50.5303	50.6756	1.0000	50.7973	1.0000	50.7661	1.0000
53.6326			53.8477	1.0000	53.6969	1.0000
77.4622			77.6671	1.0000	77.7103	1.0000
87.1822			87.6263	0.9998	87.8136	0.9997
96.2350			96.2649	0.9999	96.2576	1.0000
107.1969					107.5268	0.9998
114.3559					114.7188	0.9999
126.1380					169.4028	0.9944
137.9789					138.2839	0.9973
138.7379					140.5087	0.9973
140.3294					141.9454	0.9977

3.4.3 Variation of Residual Flexibility Values for Different Numbers of Retained Modes and Boundary Mass Sizes

It is interesting to observe the effect upon the magnitude of residual flexibility values of varying (1) boundary mass size (weight) and (2) number of mass-additive modes. Of course, the residual flexibility decreases as a function of number of retained modes, since it represents an approximation of modes not retained in the reduced model. In addition, for a given frequency bandwidth, one would expect residual flexibility associated with boundary DOFs to be smaller in the case of mass-loaded boundaries, since localized boundary modes are lowered into the bandwidth. These trends are indeed observed and are of importance because the smaller the residual flexibility values are, the more difficult it becomes to measure them with accuracy.

Table 12 shows the variation of the residual flexibility values for all six DOFs at the mass-loaded end of the $-X, -Y$ trunnion of the Shuttle payload simulator. It is noted, however, that it is unimportant which trunnion is under discussion due to symmetry of the structure. Results are shown as a function of added mass and number of retained mode shapes. As expected, little variation is seen in the residual flexibility values with the number of retained modes for zero mass loading because the localized trunnion modes occur at high frequency. However, residual flexibility values generally decrease with increased mass and number of retained mass-additive modes.

Table 12. Variation of residual flexibility values for different mass loadings and number of retained mass-additive modes.

Added Mass (lb)	Modes Retained	X Residual (in/lb)	Y Residual (in/lb)	Z Residual (in/lb)	RX Residual (rad/in-lb)	RY Residual (rad/in-lb)	RZ Residual (rad/in-lb)
0.0	10	1.0322E–05	1.3980E–03	1.4309E–03	7.4436E–05	5.5845E–05	5.5702E–05
0.5	10	1.0296E–05	1.3843E–03	1.3346E–03	7.4433E–05	5.5347E–05	5.5685E–05
5.0	10	1.0533E–05	1.2924E–03	9.1884E–04	7.4412E–05	5.2136E–05	5.5572E–05
0.0	15	4.9568E–06	1.3856E–03	1.3932E–03	7.4411E–05	5.5649E–05	5.5680E–05
0.5	15	5.0768E–06	1.3483E–03	1.1911E–03	7.4399E–05	5.2996E–05	5.5347E–05
5.0	15	1.0201E–05	5.8527E–04	1.2984E–04	7.4400E–05	2.6923E–05	3.5435E–05
0.0	20	4.7650E–06	1.3785E–03	1.3157E–03	7.4332E–05	5.4923E–05	5.5618E–05
0.5	20	4.9033E–06	6.2687E–04	6.6237E–04	7.4391E–05	3.9352E–05	3.4554E–05
5.0	20	9.8922E–06	2.1213E–06	2.5148E–06	7.2830E–05	1.7182E–05	1.5776E–05

3.4.3.1 Results for Basic Mass-Additive Method Without Residual Flexibility. Analysis was also done to provide a reference for the improved accuracy of the hybrid method in comparison to the basic mass-additive approach.[2,4] Results are first presented for the case of 0.5-lb mass loading at each trunnion of the payload simulator, with three translational DOFs to be constrained at each point (12 boundary DOFs total). It was found that 30 or more mass-additive modes are required in the absence of residual terms to derive accurate constrained modes, as shown in table 13. The precise number of mass-additive modes needed depends upon the number of constrained modes required and upon the mass size. Clearly the use of residual flexibility reduces the number of mass-additive modes that must be retained, measured, and used for model correlation.

Table 13. Derived constrained modes for the basic mass-additive method with no residual terms (0.5-lb loading, 12 boundary DOFs).

	30 Modes		40 Modes	
Exact Frequency	Derived Frequency	X Orthog. Diagonal	Derived Frequency	X Orthog. Diagonal
6.9501	6.9592	1.0000	6.9508	1.0000
9.6823	9.8883	0.9996	9.6990	1.0000
12.4921	12.4951	1.0000	12.4947	1.0000
13.7879	13.7987	1.0000	13.7906	1.0000
22.8302	22.8595	0.9997	22.8327	1.0000
28.6450	28.6501	1.0000	28.6477	1.0000
34.1967	45.1418	0.9788	35.4612	0.9995
50.5303	50.5326	1.0000	50.5322	1.0000
53.6326	53.6362	1.0000	53.6334	1.0000
77.4622	184.9571	0.4288	79.6931	0.9985
87.1822	87.1841	1.0000	87.1830	1.0000
96.2350	96.2370	1.0000	96.2351	1.0000
107.1969	107.2051	0.9999	107.1971	1.0000
114.3559	114.3574	1.0000	114.3561	1.0000
126.1380	139.4956	0.8711	139.5815	0.9173
137.9789	139.4956	0.4613	138.0498	0.9325
138.7379	138.7394	0.9994	138.7382	1.0000

For the case of 24 boundary DOFs (6 DOFs at each mass attach point), the findings are more dramatic. It was found for the 0.5-lb masses that over 100 mass-additive modes are required. If 5-lb boundary masses are used, the number of required modes is reduced, but is still on the order of 50 modes (table 14). The basic mass-additive approach without residual flexibility thus becomes impractical as the number of boundary DOFs to be constrained increases. Further, large masses may be required depending on the structure geometry and weight and, again, on the number of boundary DOFs.

Table 14. Derived constrained modes for basic mass-additive method (24 boundary DOFs).

	0.5-lb Mass				5-lb Mass			
	80 Modes		120 Modes		40 Modes		60 Modes	
Exact Frequency	Derived Frequency	*X* Orthog. Diagonal	Derived Frequency	*X* Orthog. Diagonal	Derived Frequency	*X* Orthog. Diagonal	Derived Frequency	*X* Orthog. Diagonal
9.2768	9.5214	0.9996	9.3666	1.0000	9.7064	0.9956	9.2779	1.0000
18.7627	50.2338	0.8195	19.8629	1.0000	37.8934	0.8474	18.7899	0.9999
20.6366	21.1980	0.9998	21.1155	0.9999	24.3270	0.9585	20.6458	1.0000
23.9799	26.1960	0.9986	24.7410	0.9998	27.0747	0.8692	23.9906	1.0000
32.8235	35.6061	0.9990	33.7720	0.9999	45.1629	0.7567	32.8350	1.0000
40.7146	103.1966	0.7874	42.3876	0.9996	37.8934	0.4814	41.4989	0.9993
40.8733	43.5301	0.9991	41.9371	0.9997	48.4817	0.8387	40.9150	1.0000
56.3890	57.4705	0.9987	56.7345	0.9999	66.2439	0.8393	56.3938	1.0000
60.0858	61.3925	0.9997	61.1922	0.9998	81.6551	0.5665	60.1071	1.0000
79.8798	50.2338	0.5709	80.7078	0.9999	160.7461	0.4393	80.2266	0.9995
91.6779	93.2684	0.9991	92.2803	0.9999	81.6551	0.7764	91.7013	1.0000
96.6930	96.8202	0.9998	96.7348	1.0000	97.3461	0.9863	96.6935	1.0000
107.9900	108.2658	0.9996	108.0823	1.0000	109.2487	0.9539	107.9912	1.0000
116.7489	117.6004	0.9996	117.0174	1.0000	122.2673	0.8914	116.7526	1.0000
126.1755	140.1308	0.9828	135.0474	0.9900	160.7461	0.0322	137.0175	0.9852
138.8683	103.1966	0.5971	139.2480	0.9965	160.7461	0.2484	138.9920	0.9968
141.6920	142.1686	0.9306	141.9843	0.9958	128.4337	0.6333	141.6965	1.0000
142.5079	143.5388	0.9303	142.8434	0.9958	152.4853	0.6525	142.5127	1.0000

Two other observations can be made from tables 13 and 14. First, it appears that the larger 5-lb mass, if used in the 12 boundary DOF case for the basic mass-additive method, could reduce the number of required modes to a practical level. However, this case was not investigated, and it has merit for further study. Second, it is possible that the type of boundary DOFs (rotational or translational) may be more important than the number of boundary DOFs. It seems logical that more modes would be needed for deriving constrained modes for rotational boundary DOFs than for translational boundary DOFs.

4. EXPERIMENTAL IMPLEMENTATION OF HYBRID METHOD FOR PAYLOAD SIMULATOR WITH MASS-LOADED BOUNDARIES

Demonstration of the experimental implementation of the hybrid method was accomplished by using the Shuttle payload simulator modified at one trunnion. A rectangular 0.5-lb aluminum mass having dimensions 3.5 by 3 by 0.5 in was attached to the end of the $(-X, -Y)$ trunnion, as shown in figures 9 and 10. Three triaxial accelerometers were placed at the rectangular mass center, upper right corner, and lower left corner when viewed along the positive X axis as seen in figure 11. Hammer impact excitation was applied at several points to allow measurement of both translational and rotational FRFs and residual flexibility values. In all cases, the objective was to obtain the response of the mass center point, or response point 3, as labeled in figure 11.

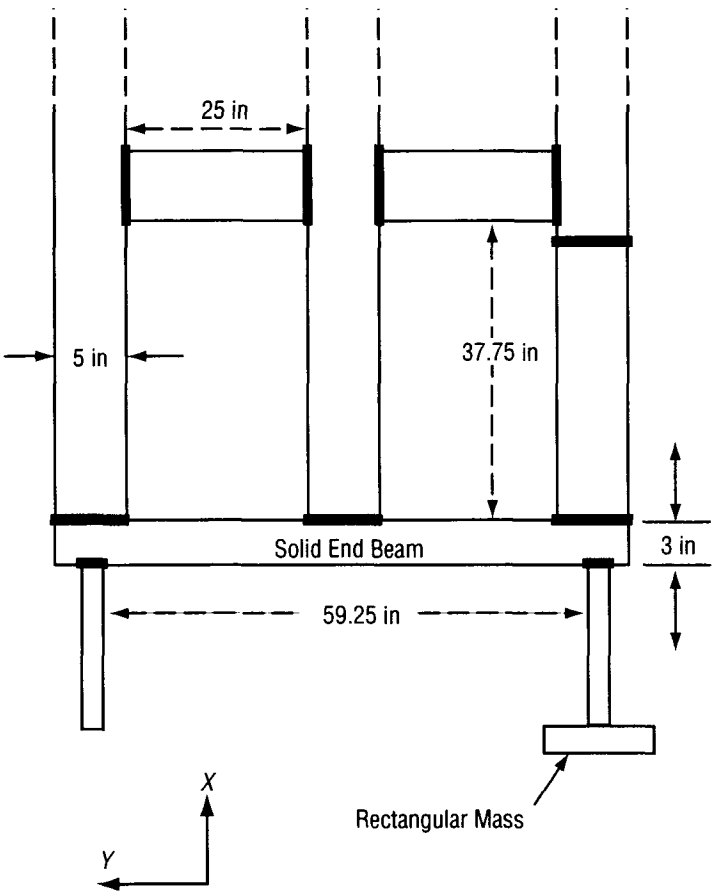

Figure 9. Payload simulator with rectangular mass attached to one trunnion.

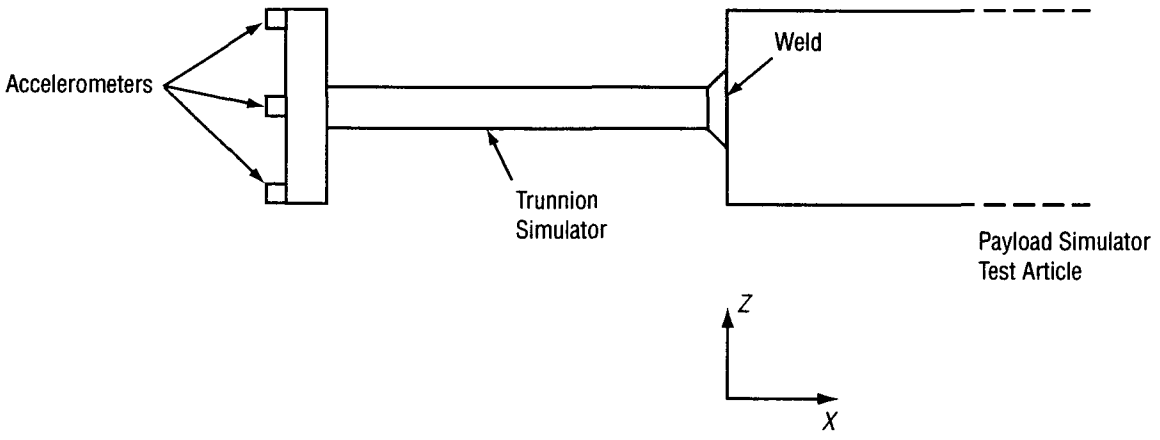

Figure 10. Detailed view of added mass and trunnion region of payload simulator.

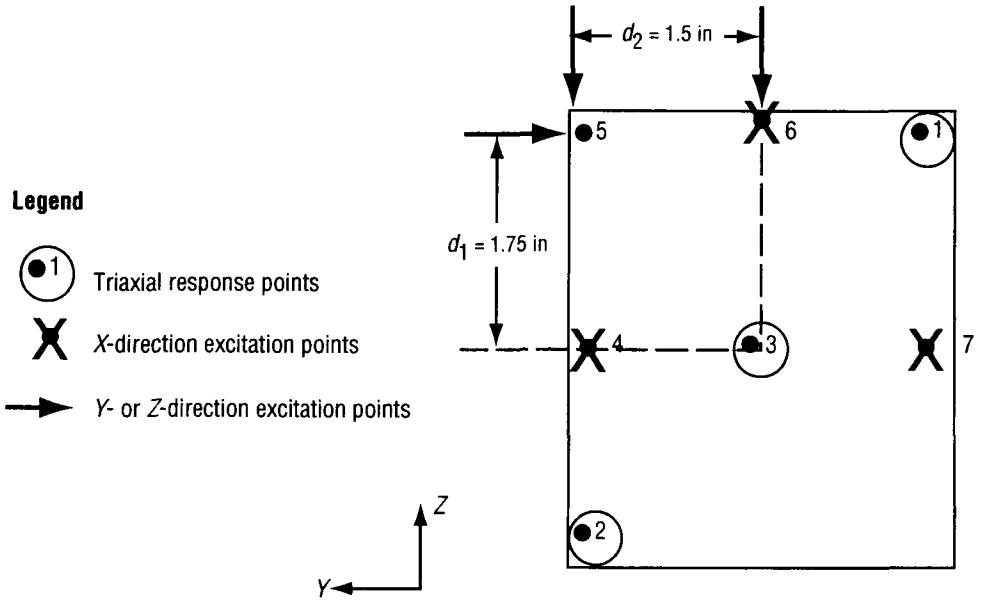

Figure 11. Rectangular mass with excitation and response points.

4.1 Translational Frequency Response Function and Residual Flexibility Measurements Compared to Analysis

For translational response of the mass center (point 3) in the X direction, excitation was applied at $6X$, and for translational Y and Z response, excitation was applied at $5Y$ and $5Z$, respectively. The excitation and response points are numbered in figure 11. The terminology for the three translational FRFs is given by the ordered pairs ($6X$, $3X$), ($5Y$, $3Y$), and ($5Z$, $3Z$) respectively. In these ordered pairs, the first entry represents the excitation point number and direction, while the second entry refers to the response point number and direction.

Figure 12 shows initial comparison of the test and analytical trunnion Y-bending response functions ($5Y$, $3Y$). A fairly large discrepancy ($\approx$8 percent for resonant frequency) existed between the model and test FRF, which required further updates to the payload simulator model. As described previously, the model without mass loading had already been updated to agree very well with measured free-free modes, frequencies, and trunnion FRFs (residuals). However, addition of the boundary mass introduced new errors and uncertainties in the model that had to be corrected. It was discovered that the discrepancy shown in figure12 was primarily due to inaccurate modeling of the trunnion-to-mass intersection. While in reality the surface of the rectangular mass was attached to the end of the trunnion, the model initially had the attach point at the center or mid-plane of the mass plate elements. For this reason, the mass attach point was in error by 0.25 in, or half the thickness of the mass. Once this was corrected by adding a 0.25 in offset in the $-X$ direction, much better agreement was obtained between the measured and predicted FRFs (fig. 13). Other refinements reflected in figure 13 include the addition of X-direction offsets for the lumped mass representations of the accelerometers, which were mounted to the outer ($-X$) surface of the rectangular mass.

Model updates for the mass-loaded trunnion FRFs were done at this stage for the two bending directions only. Previously, while investigating the basic residual flexibility method, it was found that X-direction trunnion responses were dominated by the global mode shapes rather than the stiffness of the trunnion. Very little improvement is possible by realistically modifying the trunnion axial stiffness. The Z-bending FRFs are compared for test and analysis in figure 14, and the axial (X direction) responses are shown in figure 15. It is noted that the test data at lower frequencies, below 50 Hz for the X direction and below 35 Hz for Z-bending, are not reliable near antiresonances or FRF minima. This is due to general difficulty in measuring the low response near FRF minima, which can be near the noise floor of the instrumentation. Also, the hammer tip was not soft enough to give the best response near antiresonances.

After completion of model updates for the mass-loaded trunnion to obtain acceptable agreement with test FRFs, the boundary (trunnion) residual flexibility values were compared for test and analysis. As described earlier in this TM, a residual function is defined as the difference between a full FRF based on all the structural modes and a synthesized FRF based on a subset of the modes. For example, consider a case where the full frequency response is computed or measured up to 200 Hz, but only the global modes to $\approx$85 Hz are of interest. The residual function is obtained by subtracting the synthesized FRF (based on the modes to 85 Hz) from the full FRF, as can be seen in figure 16 for the analytical ($5Y$, $3Y$) response. Note that the FRF in displacement/force format must be used. Further, as explained previously, residual flexibility is defined as the value of the residual function at zero frequency. Analytically, a residual function has zero slope at zero frequency.

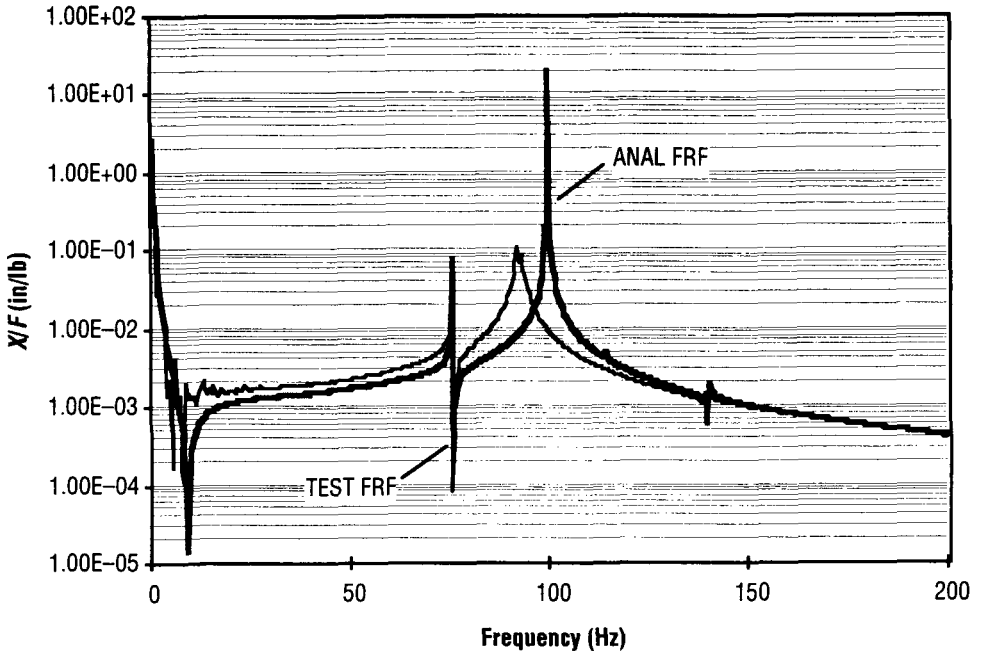

Figure 12. Initial test/analysis comparison of Y-bending responses for attached mass, excitation at mass corner point 5, response at mass center point 3 ($5Y$, $3Y$).

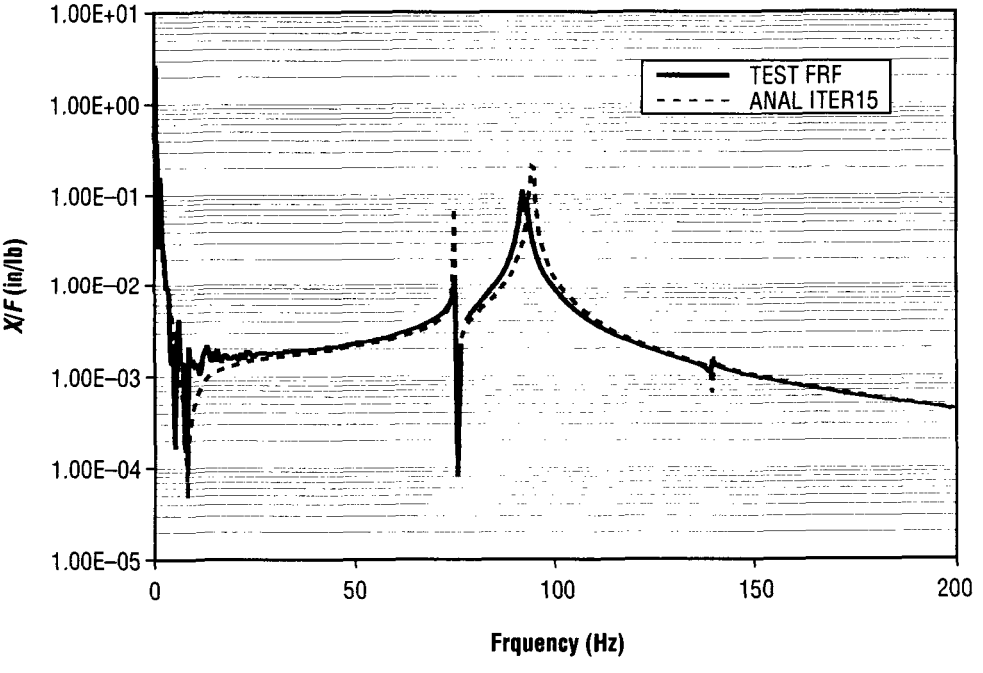

Figure 13. Comparison of test/analysis Y-bending responses ($5Y$, $3Y$) for attached mass after model updates.

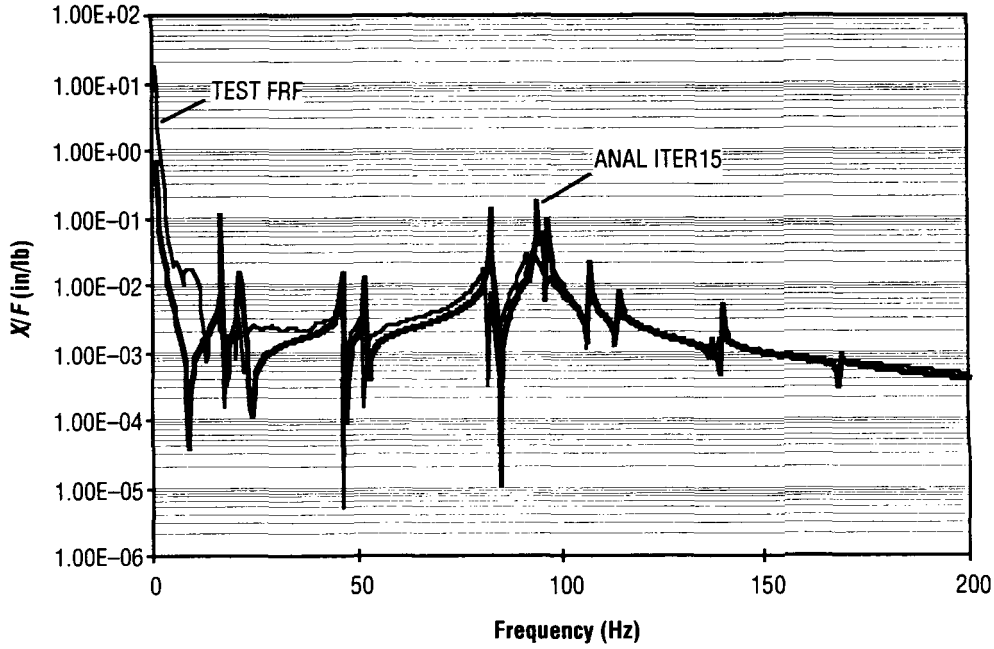

Figure 14. Comparison of test and updated analytical Z-bending responses ($5Z$, $3Z$) for attached mass.

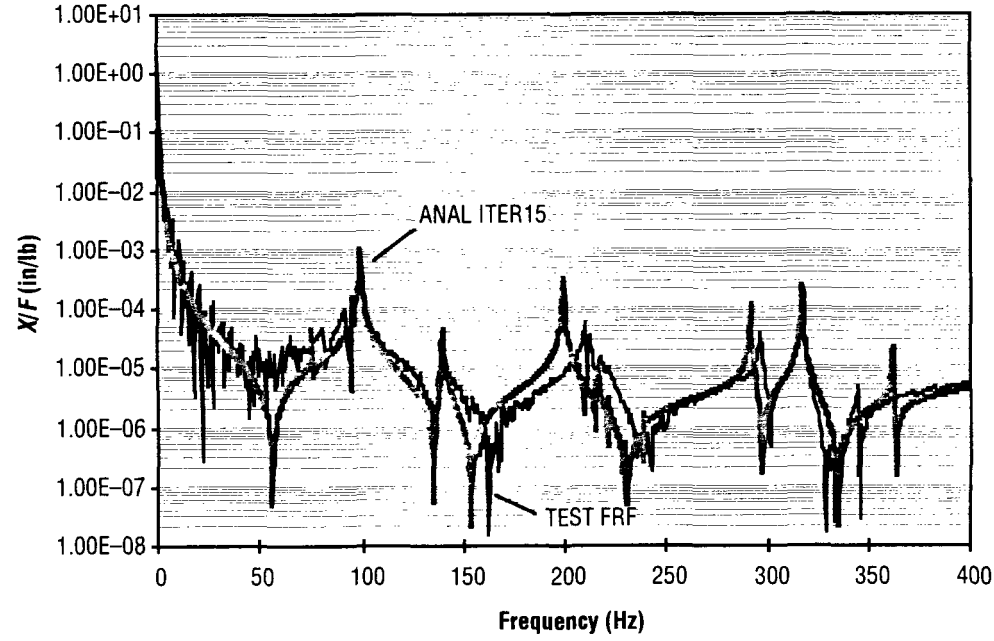

Figure 15. Measured and updated analytical axial responses ($6X$, $3X$) for attached mass.

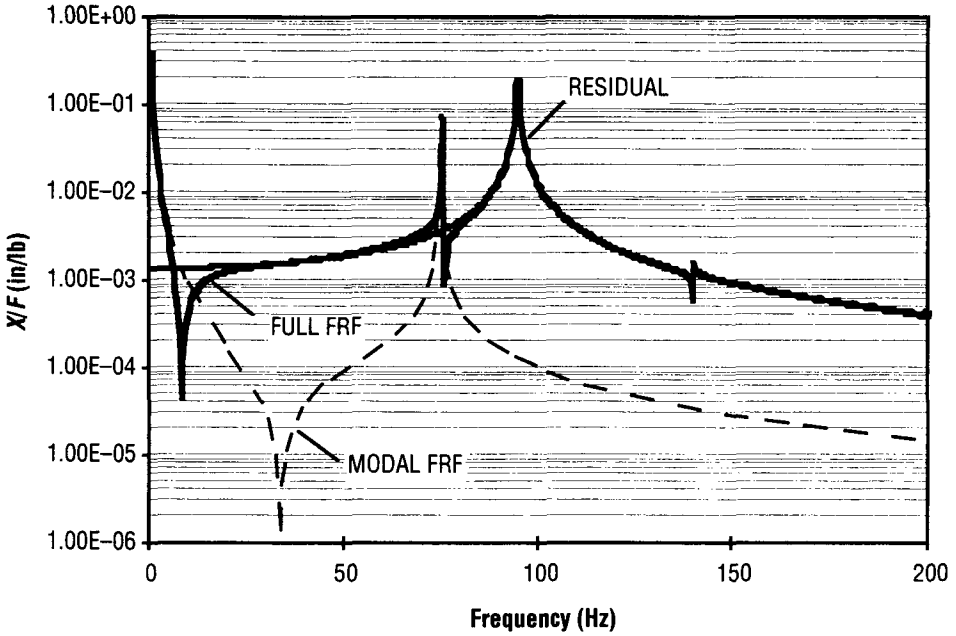

Figure 16. Analytical residual function as difference between full and modal response functions (5*Y*, 3*Y*).

Test data for the (5*Y*, 3*Y*) response functions and residual function are shown in figure 17. At low frequencies, the region most critical for determining residual flexibility values, the full FRF and the residual function are very noisy. This is overcome by performing a weighted second-order least-squares curve fit as discussed earlier in this TM. The curve-fitting procedure utilizes the fact that a theoretical residual function, or a perfectly clean measured residual function, must approach zero slope as it approaches zero frequency. In figure 17, both the residual function and a smooth curve-fitted function are shown. Statistical weighting of the data allows the noisy regions to be excluded from the smoothed curve, which therefore follows the "backbone" of the residual function. Figure 18 presents a comparison of experimental and analytical residual functions for the trunnion *Y*-bending (5*Y*, 3*Y*) response, including a smooth curve-fit of the test function. The noisy test residual data that has been weighted out by the curve fit can be clearly seen near 10 Hz. In figures 19 and 20, measured and predicted residual functions are compared for the trunnion *Z*-bending (5*Z*, 3*Z*) and axial (6*X*, 3*X*) directions, respectively. The experimental and analytical residual flexibility values for all three trunnion translational directions are given in table 15.

It must be noted at this point that a limitation exists in the current state of the art for this type of testing. In figures 20 and 21, for the trunnion *X* direction residual functions, the test data are very noisy for frequencies below ≈70 Hz. A curve approaching zero slope at zero frequency cannot be discerned, which is a requirement for obtaining accurate residual flexibility values. Figure 21 shows that even though the experimental residual flexibility value is reasonable and close to the analytical value, the least-squares curve-fitting procedure broke down. This occurred because the noisy test data actually have an upward trend below 60 Hz, not the gradual downward trend which correctly describes analytical and clean experimental residual functions. In such cases, only the FRFs can be compared with confidence in the current state of the art. Possibly, higher order curve fitting could be used to alleviate this problem.

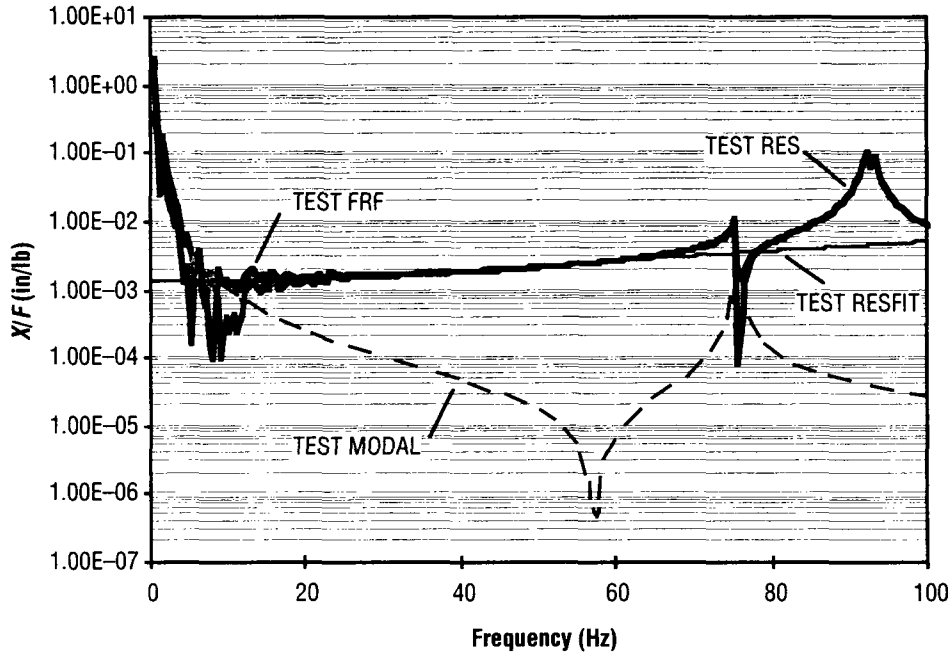

Figure 17. Test residual function and smooth curve-fitted function, shown as difference between full and synthesized response functions (5*Y*, 3*Y*) for attached mass.

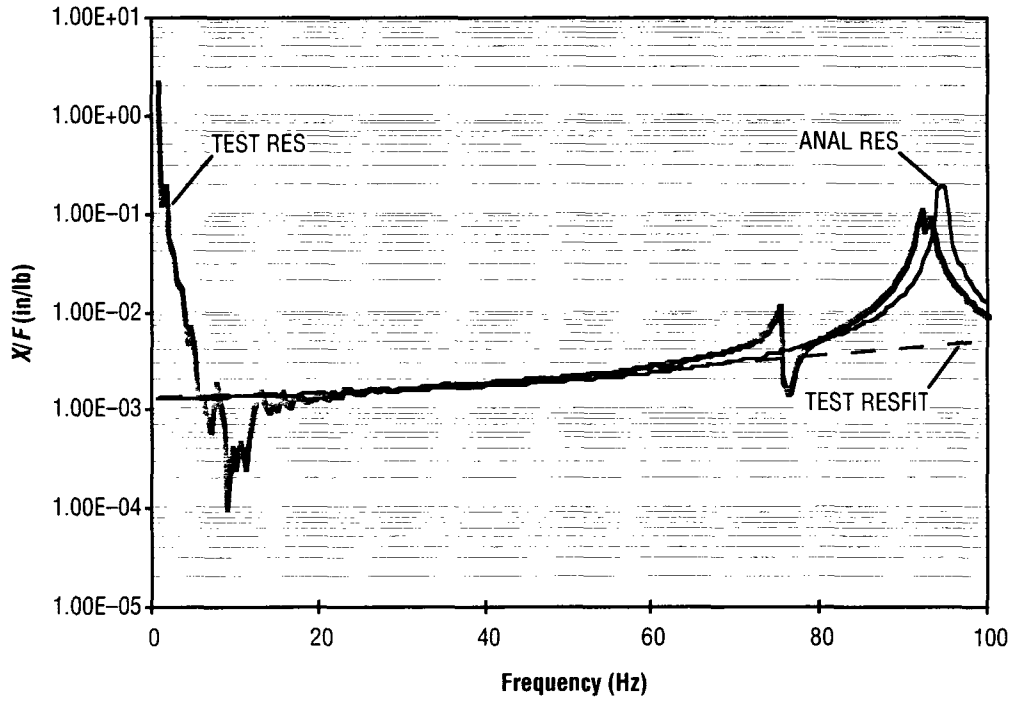

Figure 18. Comparison of test and updated model residual functions, *Y*-bending (5*Y*, 3*Y*) for attached mass.

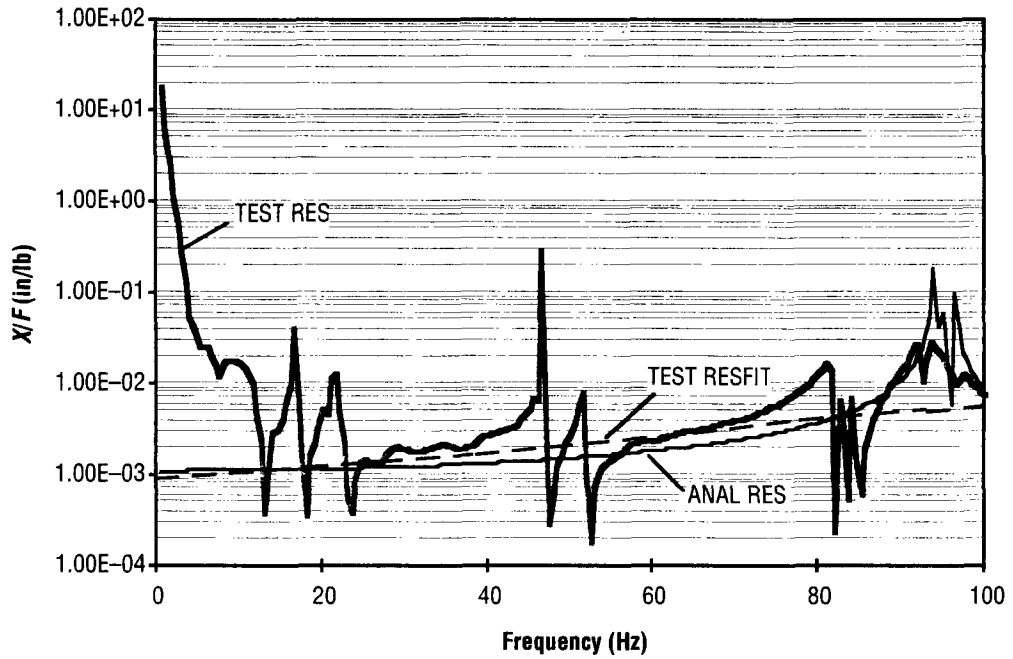

Figure 19. Measured and updated analytical residual functions for trunnion Z-bending at mass attachment location ($5Z$, $3Z$).

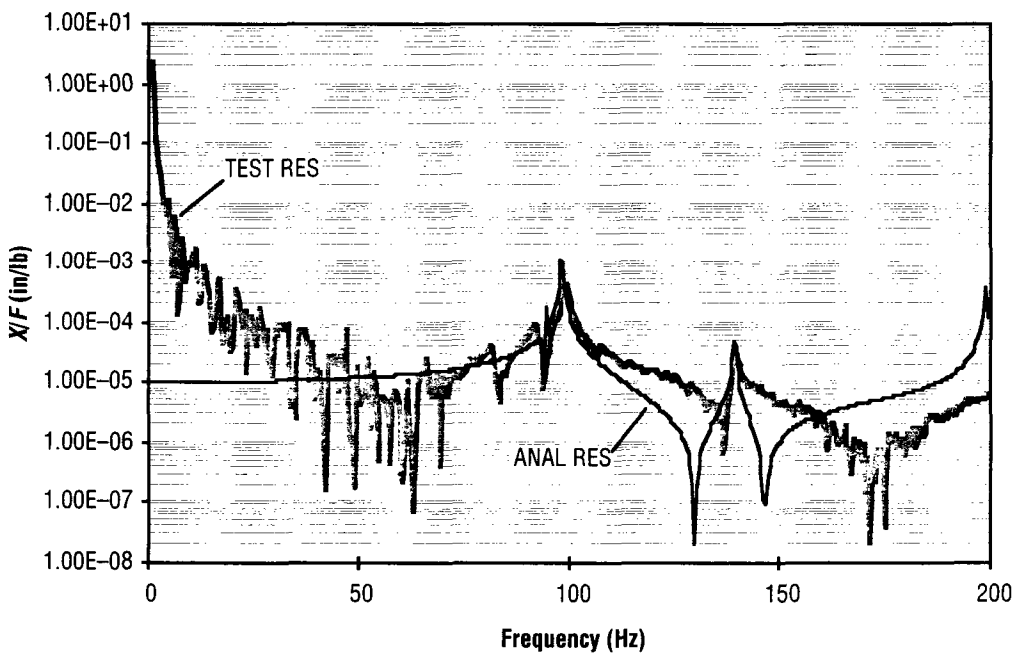

Figure 20. Residual functions from test and updated model for mass-loaded trunnion in axial direction ($6X$, $3X$).

Table 15. Residual flexibility values for test and correlated model at trunnion mass attachment location.

Direction	Location of Drive, Response	Test Residuals (in/lb, 1/in-lb)	Analysis Residuals (in/lb, 1/in-lb)
X	6*X*, 3*X*	8.7579E–06	1.0294E–05
Y	5*Y*, 3*Y*	1.3233E–03	1.4295E–03
Z	5*Z*, 3*Z*	9.5622E–04	1.1052E–03
RX		6.1642E–05	6.0524E–05
RY		3.4106E–05	5.0201E–05
RZ		4.1580E–05	5.6278E–05

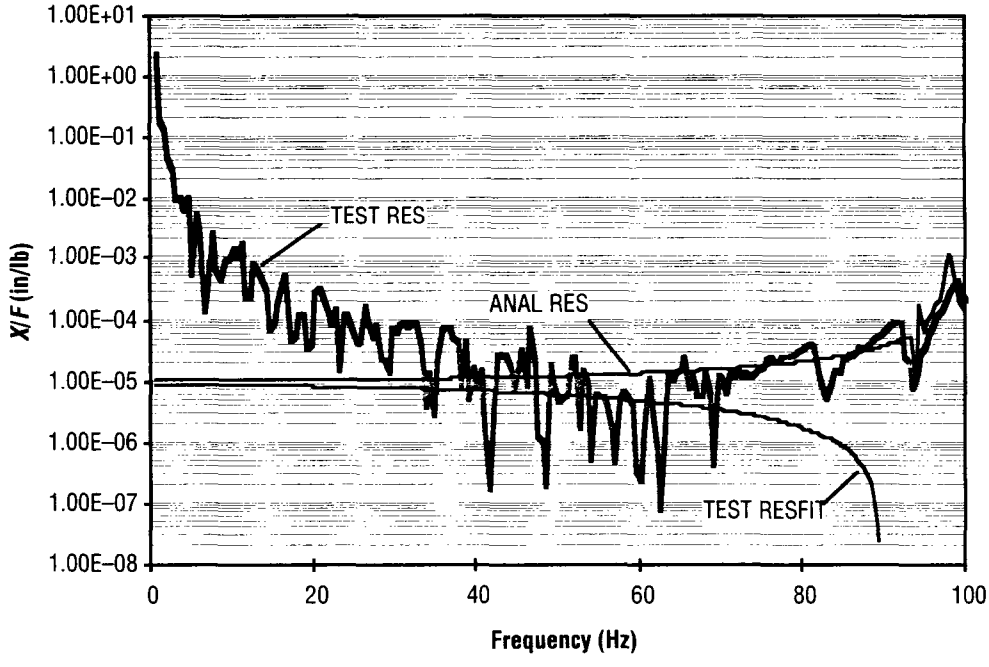

Figure 21. Residual functions from test and analysis for *X* direction (6*X*, 3*X*), showing an example of breakdown of second-order curve fit for noisy test data.

Inspection of figures 16–18 for trunnion *Y* bending shows that the residual function closely tracks the FRF except at the lowest frequencies, where the FRF is dominated by rigid-body behavior. This phenomenon points out the physical significance of residual flexibility for the payload simulator trunnions. Residual flexibility in a given coordinate is an approximation of the physical flexibility (inverse of stiffness) of the trunnion in that direction. Closed-form solutions for the stiffness and flexibility of a simple cantilever beam verified this result. This observation holds true for any structural boundary DOF. However, it is particularly obvious for a prominent flexible interface whose FRF has a dominant stiffness line, or upward-sloping trend, toward the fundamental mode of the interface structure. Such stiffness lines are especially apparent for the trunnion *Y*-bending FRF in figures 13 and 16–18.

4.2 Approximate Rotational Frequency Response Functions Derived From Translational Test Data and Comparison With Analysis

In this and the following section, the main advantages of combining mass loading of structure boundaries with the residual flexibility technique will be demonstrated. It has been stated previously in this TM that rotational measurements typically are not attempted in modal testing, mainly due to difficulties in performing the measurements in the absence of rotational sensors and due to the expense of such sensors if they are utilized. In addition, even if rotational accelerometers were available, rotational responses are typically small and difficult to measure accurately. This is particularly true for torsion if the structure has beam-like boundary regions, which is the case for the payload simulator structure.

The problem of rotational FRF and residual flexibility measurements can be at least partly alleviated using the hybrid test/analysis approach presented in this TM. The rectangular mass excitation and response points shown in figure 11 were utilized to obtain good approximations of the trunnion rotational FRF and residual functions for the payload simulator. Redundant excitation and response points were used to provide at least two approximations for each rotational FRF. In all cases, the objective was to measure response about the mass center, labeled point 3 in figure 11.

The rotational data were extracted from translational measurements using the simple arc length formula, $s = r\,\theta$. In this expression, r is the length of a line extending from a reference point to a point on a curve, θ is the angle about the reference point swept out by the line, and s is the arc length. In the case of the rectangular mass shown in figures 10 and 11, the reference point is the mass center response point, or point 3. For rotational response about an axis through the mass center and parallel to the X axis, the excitation at $5Y$ was used initially, along with the Y translational responses at points 1 and 3 (mass center and upper right corner, respectively):

$$\theta_x = RX = \frac{s}{r} = \frac{y_1 - y_3}{d_1} \quad . \tag{60}$$

It is noted that small rotations are assumed in this formulation, which is a valid assumption for the low input forces used in most modal tests. Equation (60) gives the rotational (torsional) response about an axis parallel to the X axis through the mass center point, but the standard normalized form of the FRF is needed, which is expressed as

$$\frac{\theta_x}{M_x} = \frac{RX}{MX} = \frac{y_1 - y_3}{d_1}\left(\frac{1}{F_{5y} d_1}\right) = \frac{y_1 - y_3}{F_{5y} d_1^2} \quad . \tag{61}$$

In equation (61), the moment about the mass center is $F_{5y} d_1$, the force in the Y direction applied at excitation point 5 of figure 11, multiplied by the distance to the mass center. It was desired to verify experimental results obtained by use of equation (61) by developing a second expression for the rotational FRF. In this case, excitation applied at point 5 in the Z direction was utilized along with translational responses in Z at points 2 and 3:

$$\frac{RX}{MX} = \frac{z_2 - z_3}{d_2}\left(\frac{1}{F_{5z} d_2}\right) = \frac{z_2 - z_3}{F_{5z} d_2^2} \quad . \tag{62}$$

Rotational FRF about the rectangular mass center for the other two axes were obtained in a similar manner. In the case of rotations about an axis parallel to the Y axis, excitation in the X direction at point 6 (fig. 11) was used, along with X responses at all three accelerometers, to obtain redundant expressions given in equation (63):

$$\frac{RY}{MY} = \frac{x_1 - x_3}{F_{6x} d_1^2} = \frac{x_2 - x_3}{F_{6x} d_1^2} \quad . \tag{63}$$

Finally, rotational responses about an axis parallel to the Z axis and through the rectangular mass center were expressed in terms of X-direction excitations at points 4 and 7 along with X responses at all three accelerometers, as shown in equation (64):

$$\frac{RZ}{MZ} = \frac{x_2 - x_3}{F_{4x} d_2^2} = \frac{x_1 - x_3}{F_{7x} d_2^2} \quad . \tag{64}$$

To validate the accuracy of the approximate expressions in equations (61)–(64), analytical rotational FRF extracted from translational responses were compared to exact θ/M analytical responses. Figure 22 presents such a comparison for θ_x rotations about the mass center (RX/MX), corresponding to equation (61).

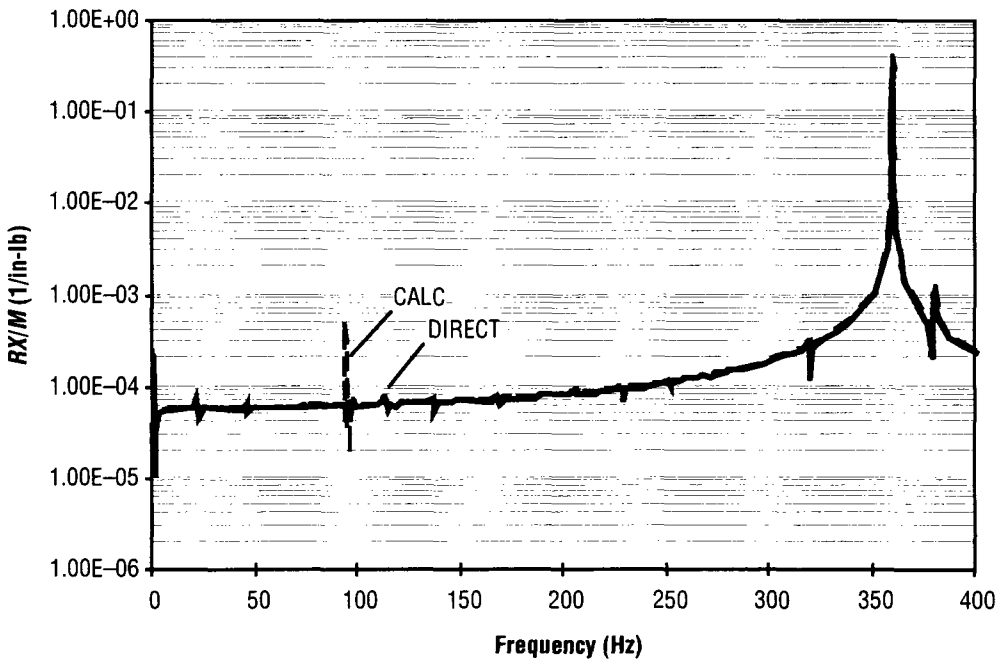

Figure 22. Rotational responses of mass ($3RX$, $3RX$), direct and calculated from translational responses.

Very little difference can be seen between the derived (dashed line) and exact (solid line) analytical response functions in figure 22. Comparisons of exact and derived θ_y and θ_z analytical rotational responses, corresponding to equations (63) and (64), are presented in figures 23 and 24.

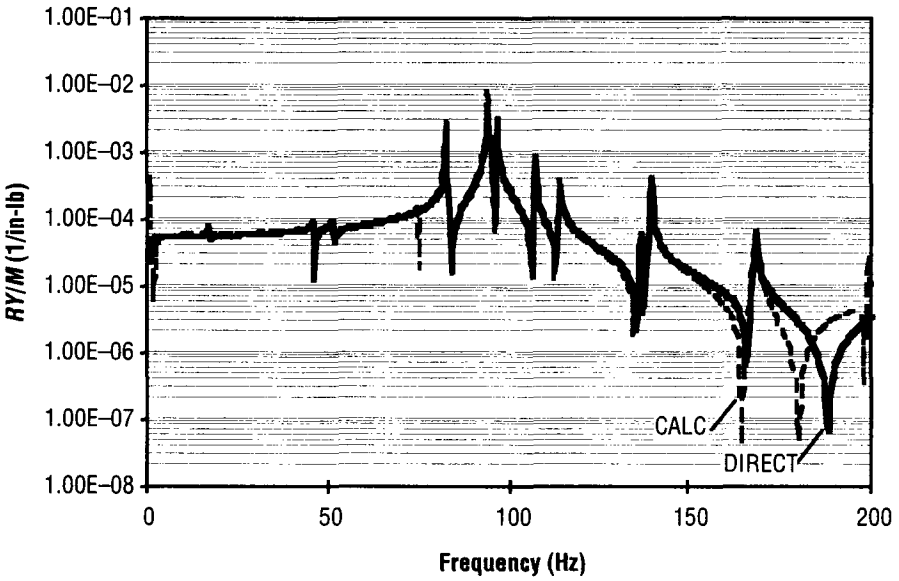

Figure 23. Comparison of direct and calculated rotational responses (3*RY*, 3*RY*) for attached mass.

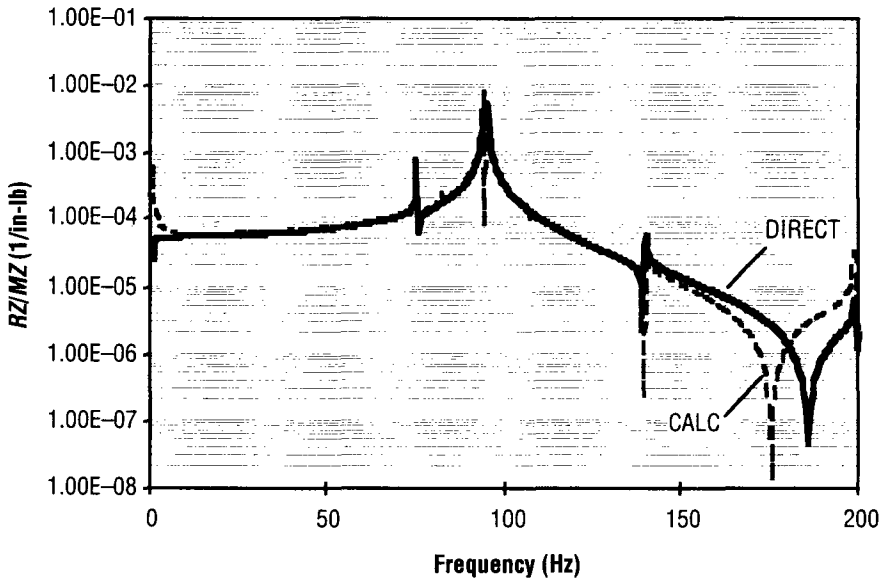

Figure 24. Direct and calculated rotational response functions (3*RZ*, 3*RZ*) for attached mass.

Differences in the derived and exact FRFs are observed in the antiresonance regions of figures 23–24 for higher frequencies. This can be explained in terms of the physical significance of a drive-point (excitation, response in same location, and DOF) response function. Antiresonances of drive-point FRF for a particular DOF correspond to the frequencies and modes that would be obtained if the structure were constrained in that DOF. Since the approximate rotational FRFs are derived from translational functions for which the excitation and response points are not coincident (non-drive-point FRFs), it should be expected that differences would exist in the antiresonances when compared to exact θ/M response functions, which are drive-point FRFs. However, since in all cases the derived rotational FRFs are virtually identical to the exact results below 140 Hz, it was concluded that the approximate rotations are sufficiently accurate. In particular, the derived functions appear accurate enough to allow estimation of residual flexibility values, which is the primary goal.

Having established acceptable accuracy of approximate rotational FRFs based on the arc length formula, experimental functions for the payload simulator were compared to results from the model. In figure 25 (a) and (b), test *RX/MX* functions derived using equations (61) and (62) are compared to the direct or "exact" analytical θ_x/M_x rotational FRFs. The computational results in figure 25 are for the final updated or correlated model that had been corrected using all available test data, including rotations. Initial model-to-test comparison of translational responses used to determine torsion (fig. 26, for example) had revealed that the finite element model in-plane torsional stiffness of the rectangular mass plate elements was drastically too low. Once this was corrected, along with increasing the trunnion torsional rigidity by about 26 percent, good agreement was achieved between model and test frequency response (fig. 27). The correlation approach was to verify all the analytical translational FRFs used in approximating the rotational responses, perform model updates as necessary, and then compare the rotational responses as the last step. Figures 28 and 29 show excellent test/analysis agreement for the *RY/MY* and *RZ/MZ* functions. Experimental rotations were obtained using both redundant calculations in equations (63) and (64).

4.3 Experimental Rotational Residual Flexibility Results and Comparison With Analysis

The final step in the implementation of the hybrid method was to estimate the rotational residual functions and residual flexibility values for the attachment point of the rectangular mass. It was stated earlier in the TM that free-suspension modal testing was done for the payload simulator structure without mass loading. Since no rotational DOFs were included in the test modal database, the normal approach for obtaining residual flexibility, subtracting a synthesized modal FRF from a full measured FRF (fig. 17, for example), could not be done for rotations as it was for translations. However, the presence of prominent stiffness lines (ramping up toward dominant local trunnion modes) in the experimental rotational FRF, as seen in figures 25, 28, and 29, made it possible to estimate residuals in an alternative fashion. A by-product of this property of the FRF is that the response function and residual function are virtually identical except at the lowest frequencies. This is also true for the translational functions, as shown in figure 17.

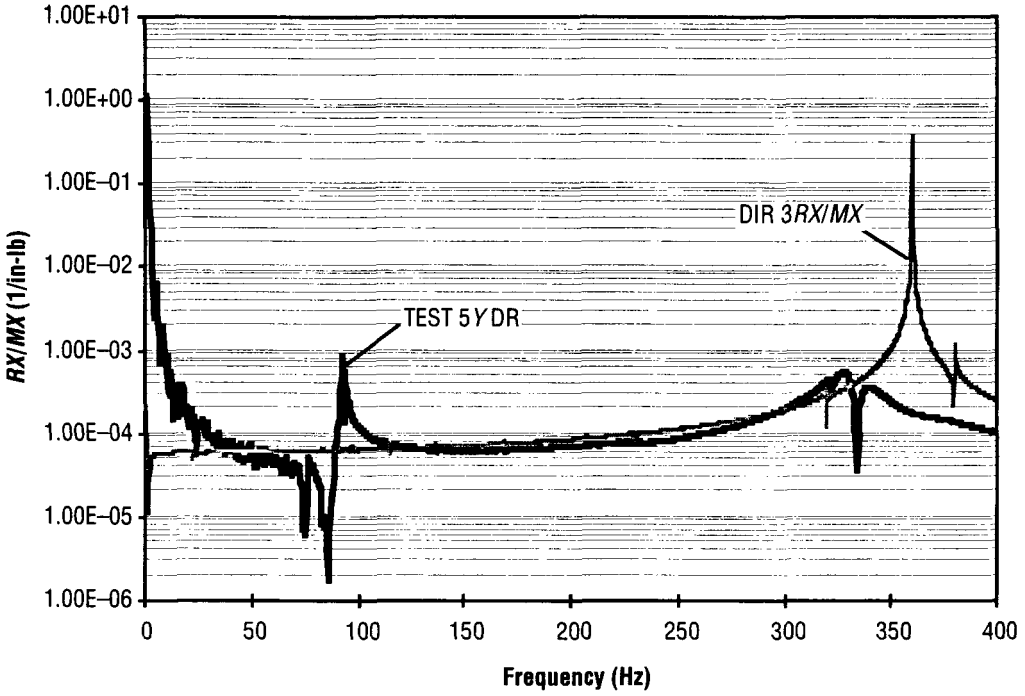

(a) Test rotational response computed from test translational data using equation (61).

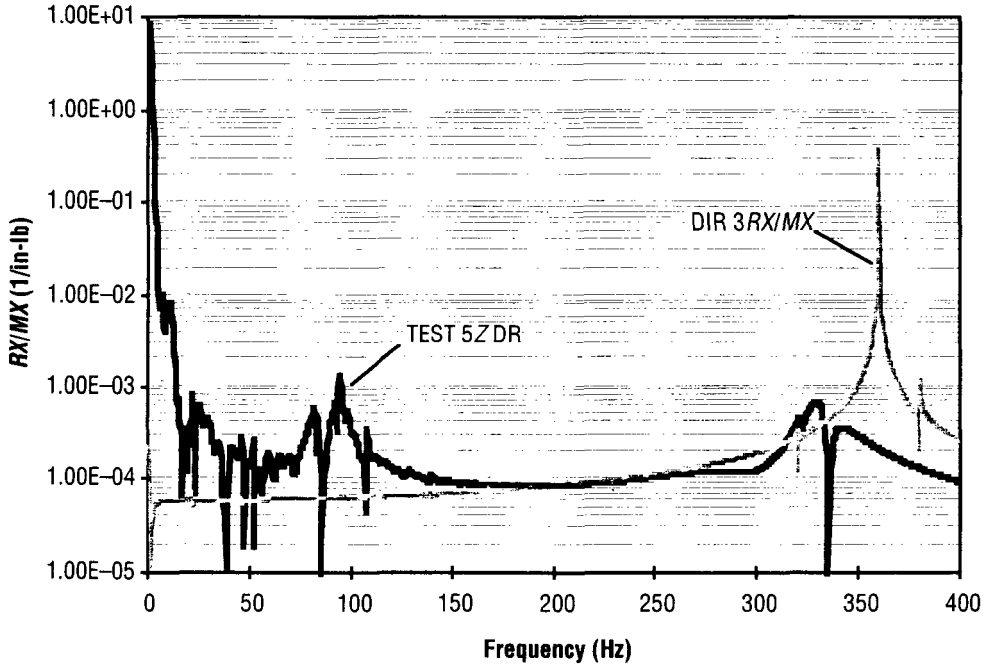

(b) Test rotational response computed from test translations using equation (62).

Figure 25. Comparison of test/analysis rotational responses about X axis at mass center ($3RX/MX$).

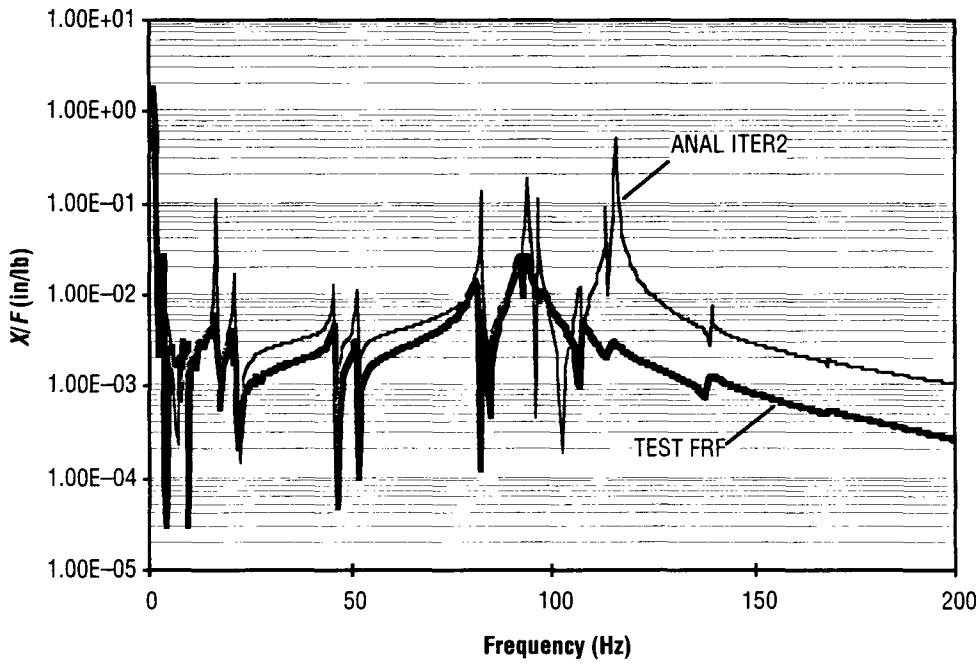

Figure 26. Test/analysis Z-bending responses ($5Z$, $2Z$) at attached mass before model updates.

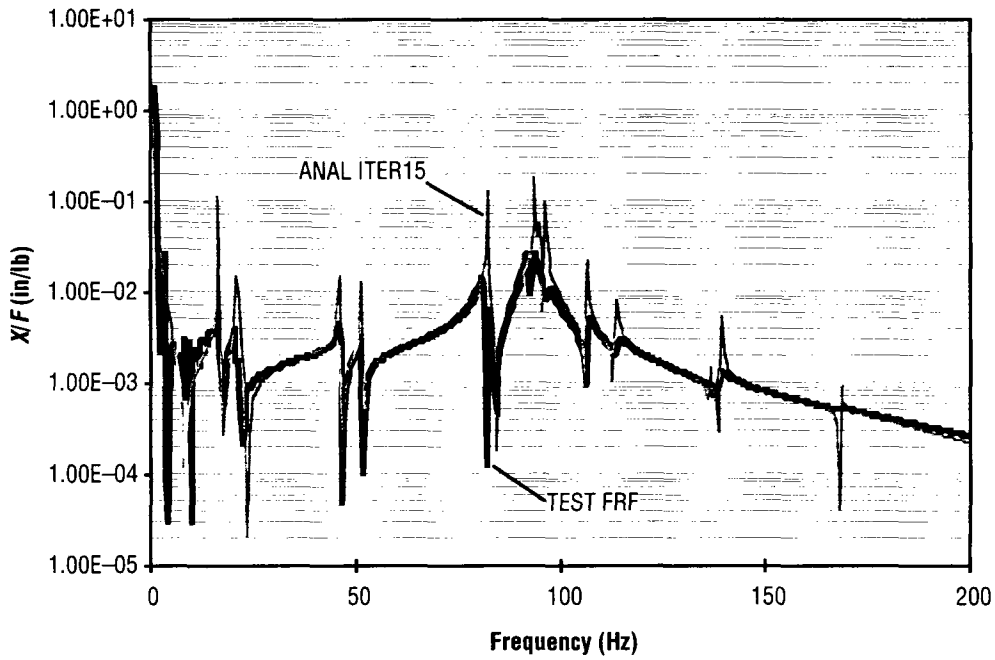

Figure 27. Test and analytical trunnion Z-bending responses ($5Z$, $2Z$) after model correlation.

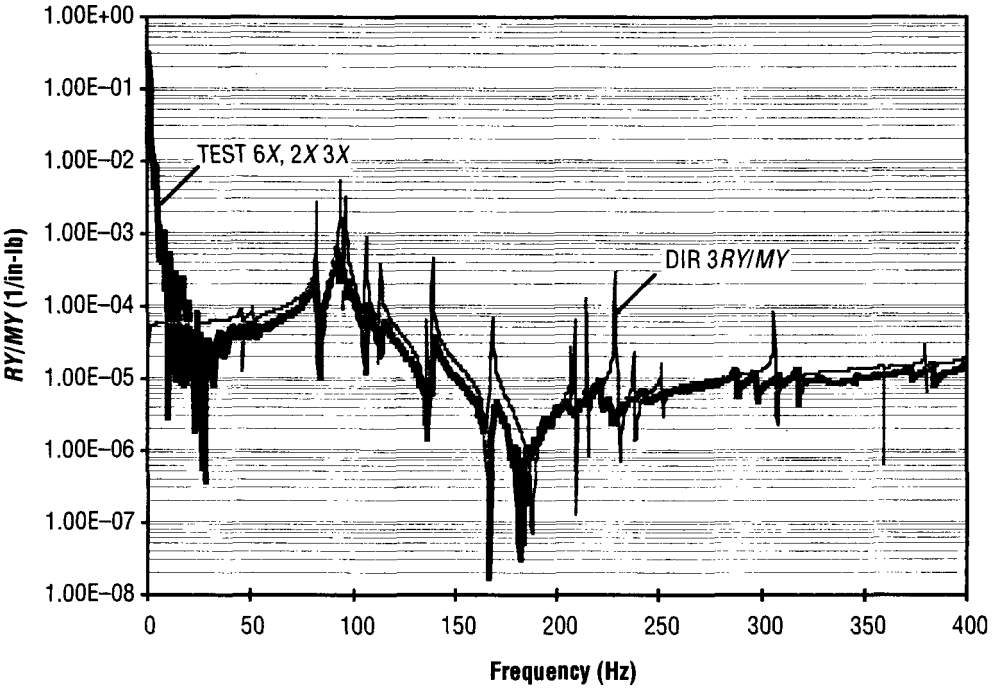

(a) Test rotational response computed from test translational data using second part of equation (63).

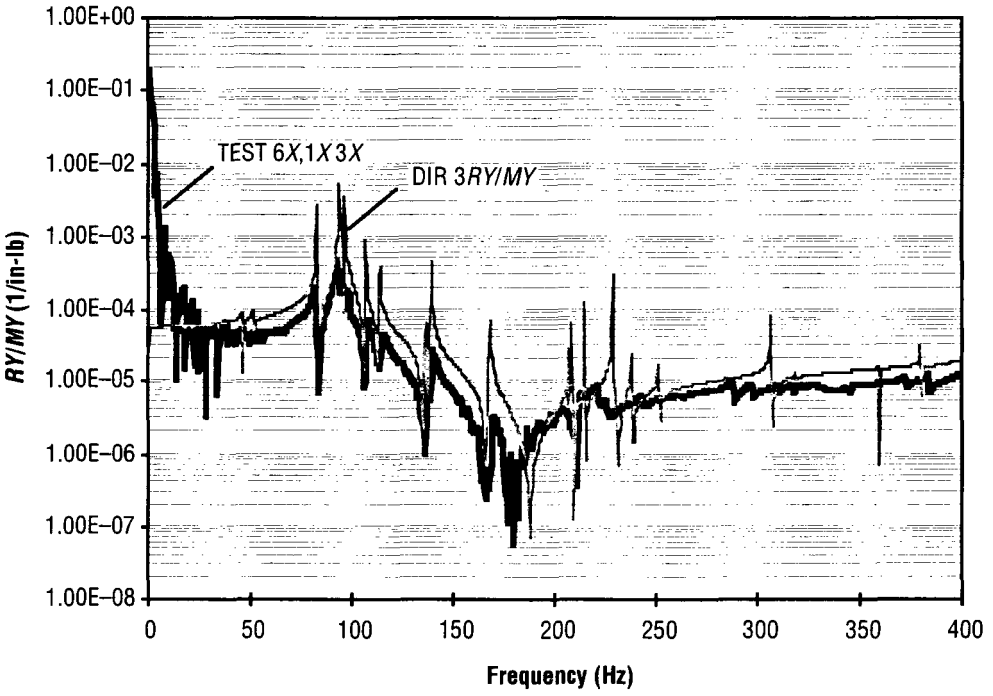

(b) Test rotational response computed from test translations of attached mass, using first part of equation (63).

Figure 28. Comparison of test and updated analytical rotations about Y axis ($3RY/MY$) at mass center.

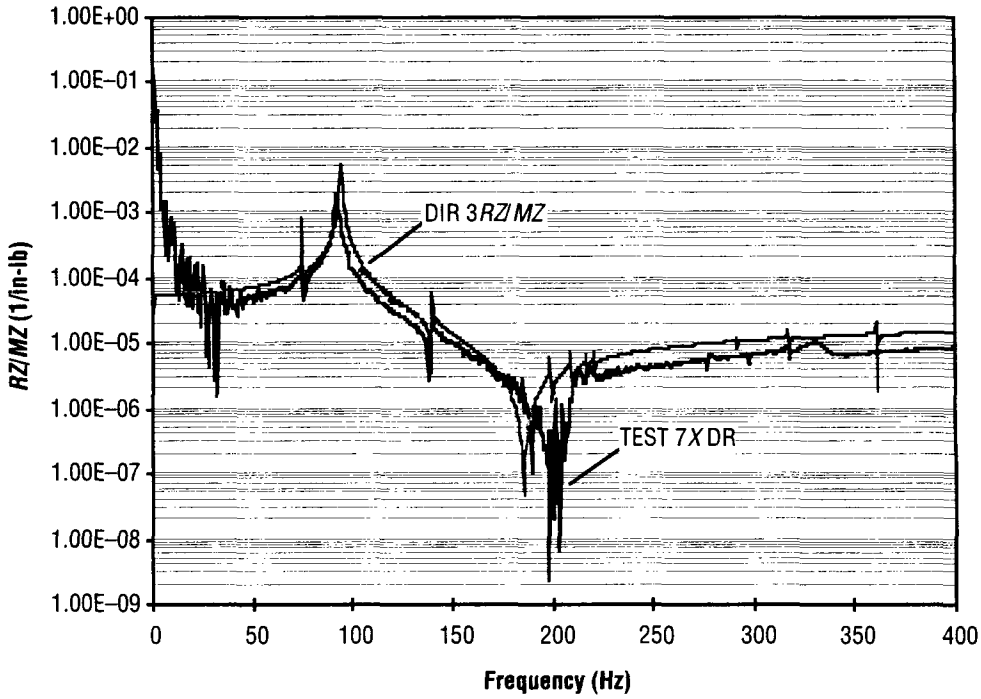

(a) Test rotational response computed from test translational data using second part of equation (64).

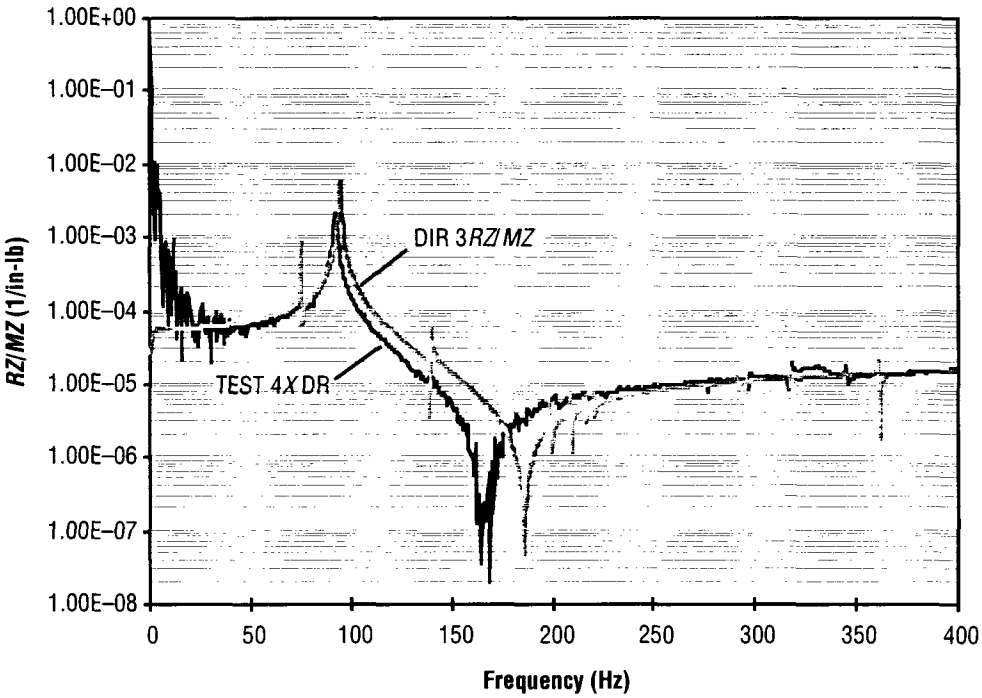

(b) Test rotational response computed from test translations, using first part of equation (64).

Figure 29. Test and updated analytical trunnion rotations about Z axis ($3RZ/MZ$) at mass center.

Because of the prominent stiffness lines in the rotational FRF, and the fact that the FRF are essentially the same as the residual functions when this occurs, the second-order least squares curve-fitting procedure that was used for translational test residual functions was applied directly to rotational FRF. Results comparing the estimated test residual functions to model predictions for *RX/MX* (θ_x/M_x) at mass point 3 are given in figure 30 (a) and (b). Figure 30 (a) corresponds to the 5*Y* excitation on the rectangular mass and equation (61), while figure 30 (b) corresponds to the 5*Z* excitation as shown in equation (62). In both parts of figure 30, the test FRFs are shown, along with a smooth curve fit of the FRF based on the prominent stiffness line region around the center of the frequency bandwidth. The analytical residual function is overlaid on the test data for comparison. For both the 5*Y* and 5*Z* excitation cases, the estimated experimental residual functions, and thus residual flexibility values, compare extremely well. Recall that residual flexibility is the value of the residual function at zero frequency.

Figure 31 compares the estimated test residual functions with analysis for *RY/MY* (θ_y/M_y) at the mass center (point 3 in figure 11). Figure 31 (a) corresponds to the first part of equation (63), where responses at mass points 1 and 3 are used, and figure 31 (b) corresponds to the second part of the equation. The agreement between test and analysis residuals is fairly good for *RY/MY* and is considered acceptable, especially in view of the good test/analysis agreement for the FRFs shown in figure 28 for a large bandwidth. Finally, the results for *RZ/MZ* at the mass center (point 3) are shown in figure 32 (a) and (b). Analysis compares extremely well with test for the 4*X* excitation case (first part of eq. (64) and fig. 32 (a)), and the comparison is acceptable for the 7*X* excitation case.

Finally, the analytical and estimated experimental residual flexibility values for rotational DOFs are shown in the lower portion of table 15. The test values are averages based on the redundant excitation and response data shown in figures 30–32 and described by equations (61)–(64). Also, the translational residual flexibilities are given in the top portion of table 15. It is noted again that in the table for the *X* direction, low confidence existed for the experimental residual value due to the lack of a prominent stiffness line and the resulting breakdown of the second-order curve fitting.

4.4 Using Models Correlated to Free-Suspension Modes and Residual Flexibility

Once the model has been updated to agree with measured free-free modes and residual terms in the mass-loaded configuration, it is a simple matter to obtain the constrained configuration. The boundary masses are removed from the finite element model, and the boundary DOFs to be constrained in service are analytically constrained.

This approach applies to the use of full models which have not been subjected to dynamic reduction. Alternatively, reduced residual flexibility models corresponding to equations (33)–(44) can be used that contain all or predominantly test-verified quantities or actual test data. Finally, as discussed previously, test-verified free-free models can be coupled to other components rather than constrained completely. This situation arises when coupled system loads analyses are to be performed.

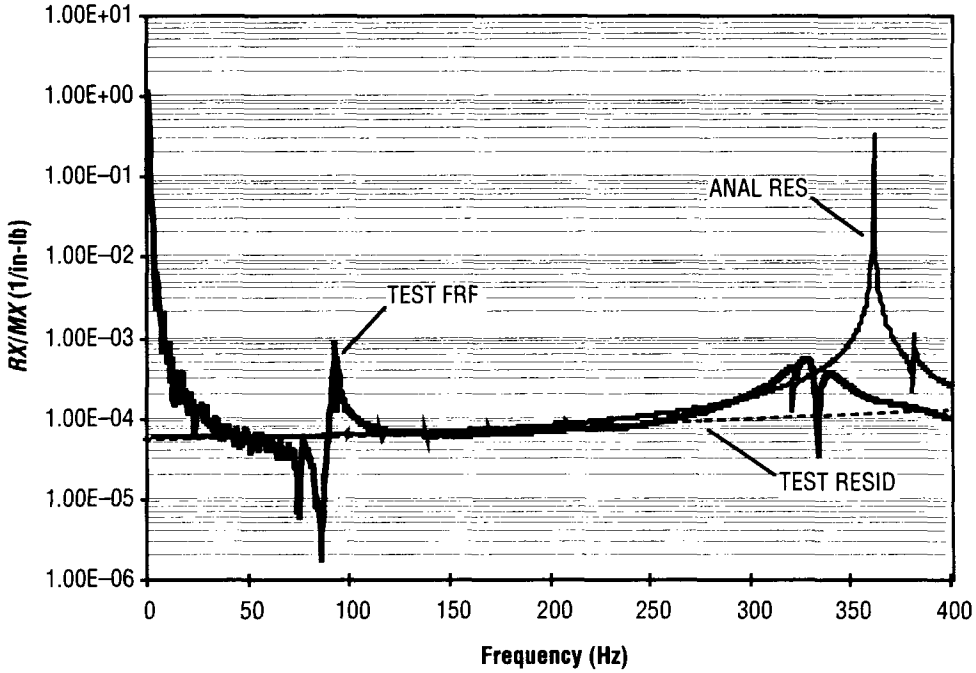

(a) Test rotational response and residual functions based on equation (61).

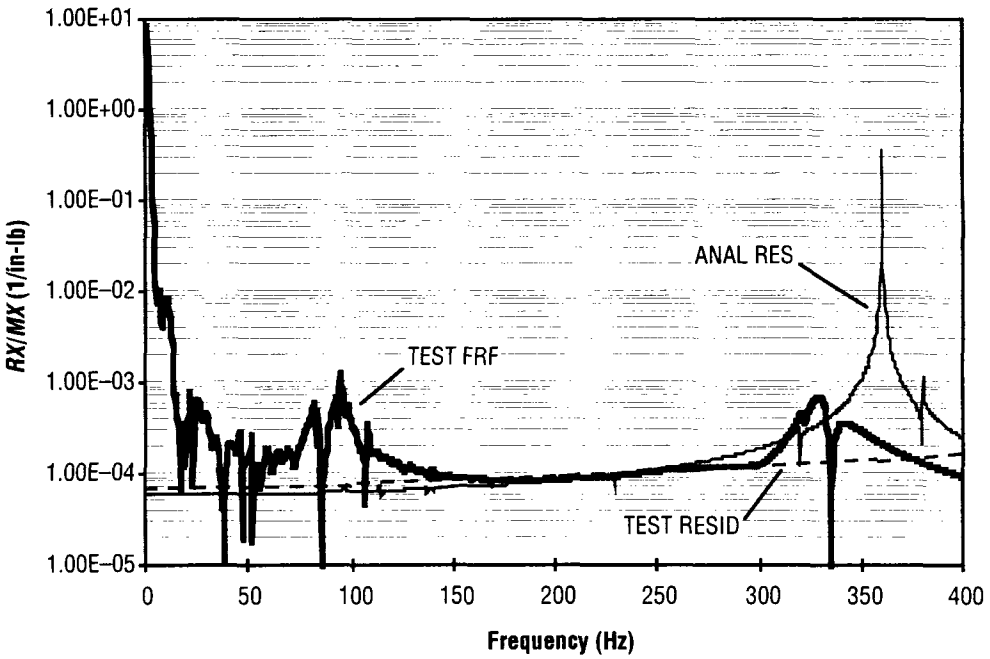

(b) Test rotational response and residual functions based on equation (62).

Figure 30. Test and updated analytical residual functions about X axis ($3RX/MX$) for attached mass.

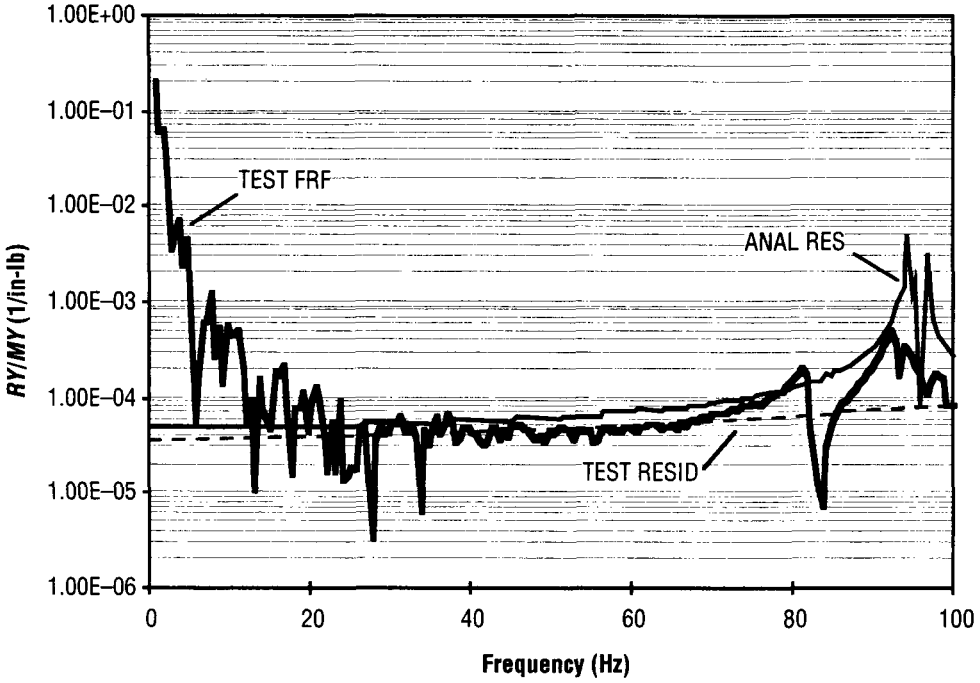

(a) Test rotational response and residual functions obtained from translations in first part of equation (63).

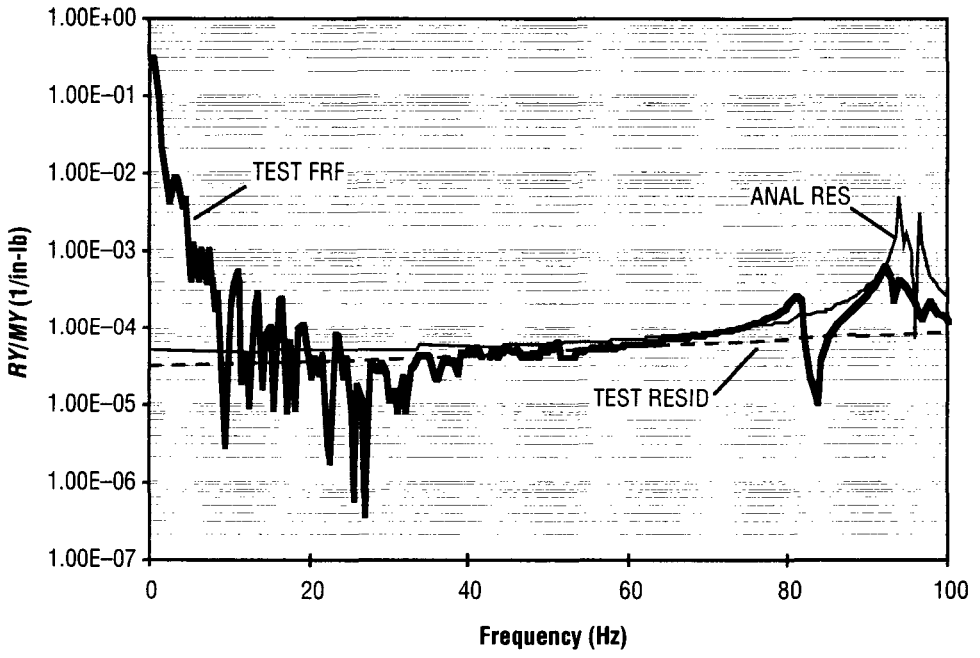

(b) Test rotational response and residual functions from test translations using second part of equation (63).

Figure 31. Test and updated analytical rotational residuals about Y axis ($3RY/MY$) at mass center.

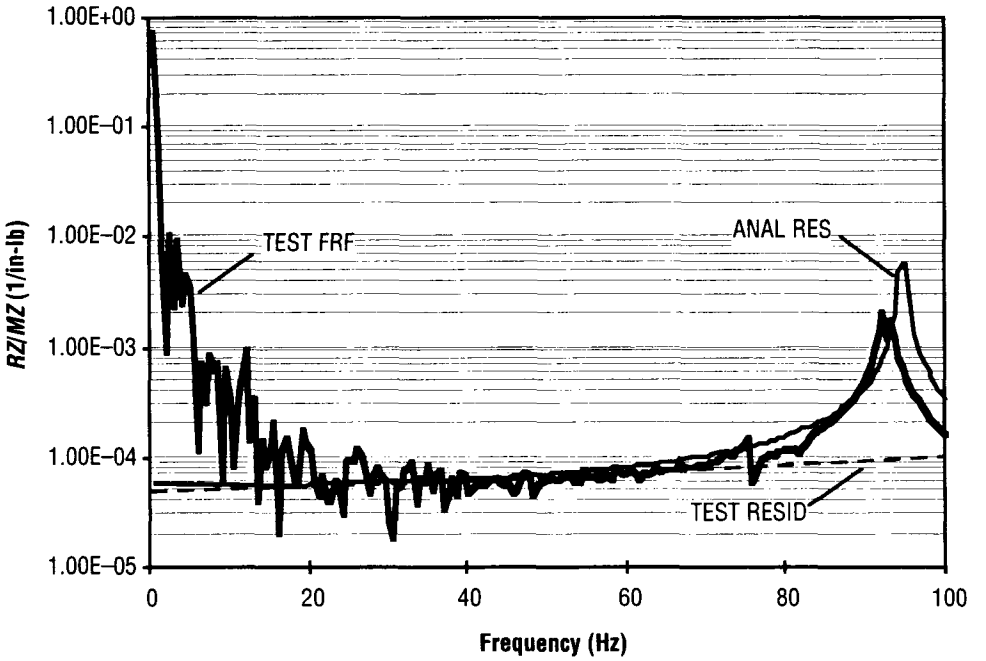

(a) Test rotational response and residual functions obtained from translations in first part of equation (64).

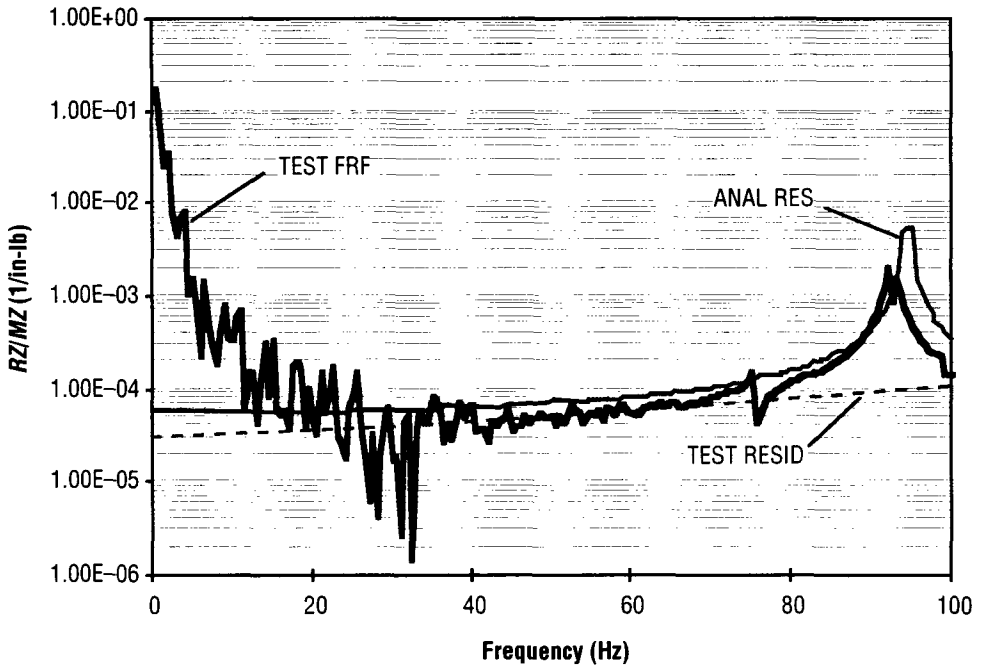

(b) Test rotational response and residual functions from test translations using second part of equation (64).

Figure 32. Test and updated analytical rotational residuals about Z axis ($3RZ/MZ$) at mass center.

5. SUMMARY

This TM has presented a thorough description and investigation of a new hybrid approach for free-suspension modal testing that allows verification of constrained-boundary structural models. The approach combines some of the best characteristics of both the residual flexibility and mass-additive techniques. The residual flexibility method alone involves the measurement of global free-free modes of the structure, along with boundary residual flexibility values, while the basic mass-additive approach involves mass loading of the structure boundaries and measurement of the free-free modes in that configuration. The hybrid approach presented in this TM combines the excellent convergence characteristics of the basic residual flexibility method with the enhancement provided by mass loading that allows measurement of rotational properties of the boundaries.

Results have been presented for a payload simulator structure showing that the hybrid method converges in a manner comparable to the basic residual flexibility method and also showing the effect of mass loading on response functions and residuals. Good agreement was demonstrated between test and analysis translational response functions and residual flexibility for the payload simulator with mass-loaded boundaries. A technique for obtaining rotational FRFs and residual functions based on the arc length formula was developed and presented in detail. Excellent agreement was obtained overall between analytical and experimental rotational FRFs and residuals.

In practical implementation of the method, the following approach should be taken: (1) Perform a free-suspension modal test in the mass-loaded configuration to obtain global modes and natural frequencies; (2) measure translational and rotational drive-point FRF and residual functions; (3) update the finite element model to agree with test modal, FRF, and residual data, typically striving for frequency errors under 5 percent for modes and FRF and diagonal cross-orthogonality values 0.90 or greater; and (4) constrain the test-correlated model or couple it to other structural components at the boundary DOF. Alternatively, and perhaps ideally, a reduced model (residual flexibility model) consisting mostly or entirely of test-verified modes and residual terms could be developed after step (3) and before step (4). This approach could be needed in cases where large finite element models are being coupled to other components and then used for transient loads analysis.

The work presented in this TM should advance free-suspension residual flexibility testing by making it more applicable to general boundary conditions and situations where rotational DOFs must be included. Though the development was based on the use of translational measurements to estimate rotational data, the technique could be used somewhat more easily in cases where rotational accelerometers are available. However, even as rotational sensors become more reliable and affordable, it is likely that the use of mass loading will always be needed to amplify the rotational responses and allow application of moments at the structure boundaries.

REFERENCES

1. Tinker, M.L.: "Modal Vibration Test Facilities and Methods for Space Station Modules," *AIAA–95–1295, Proceedings of 36th Structures, Structural Dynamics and Materials Conference*, New Orleans, LA, pp. 1190–1197, April 10–13, 1995.

2. Coleman, A.D.: "A Mass Additive Technique for Modal Testing as Applied to the Space Shuttle ASTRO–1 Payload," *Proceedings of the Sixth International Modal Analysis Conference*, Kissimmee, FL, pp. 154–159, February 1988.

3. Kinney, T.L.: "Material Science Laboratory (MSL) Carrier Modal Survey Test Summary and Model Correlation," *PMIC–RPT–6925*, Teledyne Brown Engineering, June 1990.

4. Admire, J.R.; Tinker, M.L.; and Ivey, E.W.: "Mass-Additive Modal Test Method for Verification of Constrained Structural Models," *AIAA Journal*, Vol. 31, No. 11, pp. 2148–2153, November 1993.

5. Goldenberg, S.; and Shapiro, M.: "A Study of Modal Coupling Procedures for the Space Shuttle," *NASA CR–112252*, April 1973.

6. Gwinn, K.W.; Lauffer, J.P.; and Miller, A.K.: "Component Mode Synthesis Using Experimental Modes Enhanced by Mass Loading," *Proceedings of the Sixth International Modal Analysis Conference*, Kissimmee, FL, pp. 1088–1093, February 1988.

7. Yasuda, C.; Riehle, P.J.; Brown, D.L.; and Allemang, R.J.: "An Estimation Method for Rotational Degrees of Freedom Using a Mass-Additive Technique," *Proceedings of the Second International Modal Analysis Conference*, Orlando, FL, pp. 877–886, 1984.

8. Barney, P.S.: "Investigation of Mass Additive Testing for Experimental Modal Analysis," *Ph.D. Dissertation*, University of Cincinnati, College of Engineering; Final Report for NASA Grant NAG8–170M, 1992.

9. Benfield, W.A.; and Hruda, R.F.: "Vibration Analysis of Structures by Component Mode Substitution," *AIAA Journal*, Vol. 9, No. 7, pp. 1255–1261, July 1971.

10. Admire, J.R.; Tinker, M.L.; and Ivey, E.W.: "Residual Flexibility Test Method for Verification of Constrained Structural Models," *AIAA Journal*, Vol. 32, No. 1, pp. 170–175, January 1994.

11. MacNeal, R.H.: "A Hybrid Method of Component Mode Synthesis," *Computers and Structures*, Vol. 1, pp. 581–601, 1971.

12. Rubin, S.: "Improved Component Mode Representation for Structural Dynamic Analysis," *AIAA Journal*, Vol. 13, Palm Springs, CA, pp. 995–1006, 1975.

13. Martinez, D.R.; Carne, T.G.; and Miller, A.K.: "Combined Experimental/Analytical Modeling Using Component Mode Synthesis," *Proceedings of the 25th Structures, Structural Dynamics and Materials Conference*, Palm Springs, CA, pp. 140–152, May 14–18, 1984.

14. Craig, R.R., Jr.; and Chang, C.-J.: "On the Use of Attachment Modes in Substructure Coupling for Dynamic Analysis," *Proceedings of the 18th Structures, Structural Dynamics and Materials Conference*, San Diego, CA, pp. 89–99, March 21–23, 1977.

15. Craig, R.R., Jr.: "A Review of Time-Domain and Frequency-Domain Component Mode Synthesis Methods," *Combined Experimental/Analytical Modeling of Dynamic Structural Systems*, AMD–Vol. 67, American Society of Mechanical Engineers, New York, pp. 1–30, 1985.

16. Kammer, D.C.; and Baker, M.: "A Comparison of the Craig-Bampton and Residual Flexibility Methods for Component Substructure Representation," *Proceedings of the 26th Structures, Structural Dynamics and Materials Conference*, Orlando, FL, pp. 699–706, April 15–17, 1985.

17. Blair, M.A.: "Space Station Module Prototype Test Report: Free-Free Testing Methods," EM ATTIC 001, Lockheed Missiles and Space Company, Sunnyvale, CA, June 1991.

18. Chandler, K.O.; Driskill, T.C.; and Lindner, J.L.: "Space Station Module Alternative Testing Techniques for Interface Characterization: Free-Free Modal Survey Test Report," *SS–DEV–ED90–061*, NASA Marshall Space Flight Center, Huntsville, AL, October 1990.

19. Flanigan, C.C.: "Test-Analysis Correlation of the Transfer Orbit Stage Modal Survey," *Report 40864–8*, SDRC, Inc., San Diego, CA, October 1988.

20. Smith, K.; and Peng, C.Y.: "SIR-C Antenna Mechanical System Modal Test and Model Correlation Report," *JPL D–10694*, Jet Propulsion Laboratory, Vol. 1, April 1993.

21. Klosterman, A.L.; and Lemon, J.R.: "Dynamic Design Analysis via the Building Block Approach," *Shock and Vibration Bulletin*, No. 42, Part 1, pp. 97–104, January 1972.

22. Bookout, P.S.: "Statistically Generated Weighted Curve Fit of Residual Functions for Modal Analysis of Structures," *NASA TM 108481*, February 1995.

23. Tinker, M.L.; and Bookout, P.S.: "Measurement of Residual Flexibility for Substructures Having Prominent Flexible Interfaces," *Proceedings of 35th Structures, Structural Dynamics and Materials Conference*, Hilton Head, SC, pp. 1944–1958, April 18–20, 1994.

24. Tinker, M.L.: "Free-Suspension Residual Flexibility Testing of Space Station Pathfinder: Comparison to Fixed-Base Results," *AIAA–98–1791, Proceedings of 39th Structures, Structural Dynamics and Materials Conference*, Long Beach, CA, April 20–23, 1998.

25. Tinker, M.L.; and Cutchins, M.A.: "Model Correlation Issues in Residual Flexibility Testing," *Proceedings of 1997 ASME Design Engineering Technical Conferences, DETC97/VIB–4262*, Sacramento, CA, Sept. 14–17, 1997.

26. Blair, M.A.; and Vadlamudi, N.: "Constrained Structural Dynamic Model Verification Using Free Vehicle Suspension Testing Methods," *Proceedings of the 29th Structures, Structural Dynamics and Materials Conference*, Williamsburg, VA, pp. 1187–1193, April 18–20, 1988.

27. Chandler, K.O.; and Tinker, M.L.: "A General Mass-Additive Method for Component Mode Synthesis," *AIAA–97–1381, Proceedings of 38th Structures, Structural Dynamics and Materials Conference*, Kissimmee, FL, April 7–10, 1997.

28. Craig, R.R.; and Bampton, M.C.C.: "Coupling of Substructures for Dynamic Analyses," *AIAA Journal*, Vol. 6, No. 7, pp. 1313–1319, 1968.

REPORT DOCUMENTATION PAGE

Form Approved
OMB No. 0704-0188

1. AGENCY USE ONLY *(Leave Blank)*	2. REPORT DATE	3. REPORT TYPE AND DATES COVERED
	March 2003	Technical Memorandum

4. TITLE AND SUBTITLE

Hybrid Residual Flexibility/Mass-Additive Method for Structural Dynamic Testing

5. FUNDING NUMBERS

6. AUTHORS

M.L. Tinker

7. PERFORMING ORGANIZATION NAMES(S) AND ADDRESS(ES)

George C. Marshall Space Flight Center
Marshall Space Flight Center, AL 35812

8. PERFORMING ORGANIZATION REPORT NUMBER

M—1071

9. SPONSORING/MONITORING AGENCY NAME(S) AND ADDRESS(ES)

National Aeronautics and Space Administration
Washington, DC 20546–0001

10. SPONSORING/MONITORING AGENCY REPORT NUMBER

NASA/TM—2003–212343

11. SUPPLEMENTARY NOTES

Prepared for Structures, Mechanics, and Thermal Department, Engineering Directorate

12a. DISTRIBUTION/AVAILABILITY STATEMENT

Unclassified-Unlimited
Subject Category 39
Nonstandard Distribution

12b. DISTRIBUTION CODE

13. ABSTRACT *(Maximum 200 words)*

A large fixture was designed and constructed for modal vibration testing of *International Space Station* elements. This fixed-base test fixture, which weighs thousands of pounds and is anchored to a massive concrete floor, initially utilized spherical bearings and pendulum mechanisms to simulate Shuttle orbiter boundary constraints for launch of the hardware. Many difficulties were encountered during a checkout test of the common module prototype structure, mainly due to undesirable friction and excessive clearances in the test-article-to-fixture interface bearings. Measured mode shapes and frequencies were not representative of orbiter-constrained modes due to the friction and clearance effects in the bearings. As a result, a major redesign effort for the interface mechanisms was undertaken. The total cost of the fixture design, construction and checkout, and redesign was over $2 million.

Because of the problems experienced with fixed-base testing, alternative free-suspension methods were studied, including the residual flexibility and mass-additive approaches. Free-suspension structural dynamics test methods utilize soft elastic "bungee" cords and overhead frame suspension systems that are less complex and much less expensive than fixed-base systems. The cost of free-suspension fixturing is on the order of tens of thousands of dollars, as opposed to millions, for large fixed-base fixturing. In addition, free-suspension test configurations are portable, allowing modal tests to be done at sites without modal test facilities. For example, a mass-additive modal test of the ASTRO–1 Shuttle payload was done at the Kennedy Space Center launch site. In this Technical Memorandum, the mass-additive and residual flexibility test methods are described in detail. A discussion of a hybrid approach that combines the best characteristics of each method follows and is the focus of the study.

14. SUBJECT TERMS

structural dynamics, modal testing, free-suspension methods, modal coupling, component mode synthesis, dynamic model verification

15. NUMBER OF PAGES

72

16. PRICE CODE

17. SECURITY CLASSIFICATION OF REPORT	18. SECURITY CLASSIFICATION OF THIS PAGE	19. SECURITY CLASSIFICATION OF ABSTRACT	20. LIMITATION OF ABSTRACT
Unclassified	Unclassified	Unclassified	Unlimited